



TECHNISCHE
UNIVERSITÄT
WIEN

Vienna University of Technology

DIPLOMARBEIT

Chemical potential variations in thermoelectrics

Ausgeführt am Institut für Festkörperphysik
der Technischen Universität Wien

unter der Anleitung von
Univ.Prof. Dipl.-Phys. Dr.rer.nat. Karsten Held
Projektass.(FWF) Marco Battiato, PhD

durch

Michael Wais, BSc

Matrikelnummer 1026319
Geibelgasse 12/17, 1150 Wien

Wien, am 12. September 2016

Michael Wais, BSc

Abstract

Thermoelectric materials have been a fascinating field of research ever since their first exploration. Due to their capability to convert excess heat into electrical energy in a clean and sustainable way they could be of great importance for future technologies. In order to build more efficient thermoelectric devices it is crucial to get a thorough understanding of the complex interplay of the different mechanisms within a thermoelectric material. Especially materials with large power producing capabilities can show transport coefficients which strongly depend on the temperature as well as on the position of the chemical potential. There have been several studies which include the temperature dependence explicitly but none including the chemical potential at the same level.

In this work we solve the macroscopic transport equations with their full temperature and chemical potential dependences and discuss the impact of this extended treatment on the efficiency. For that reason we derive suitable equations and boundary conditions for junctions between different materials.

We apply these equations to a full two-leg device consisting of two active regions with arbitrary materials connected by two metallic regions. We show that the equations which describe the different active regions can be decoupled which strongly reduces the complexity of the problem. We build a simulation that solves the remaining non-linear differential equations iteratively and determines the efficiency from the calculated temperature- and chemical potential distribution. As the program will be made available freely we also build a graphical user interface in order to improve the usability. We show simulation results for three materials i.e. Bi_2Te_3 , SrTiO_3 and FeSb_2 and compare the simulated efficiencies with methods to analytically estimate the efficiency.

We find that the chemical potential can be far away from its equilibrium value at the junctions due to the formation of Schottky contacts which, in some cases, dramatically decreases the efficiency. This effect has been neglected in thermoelectrics in the past which might have led to the discard of promising materials.

Additionally we build a numerical routine which allows to calculate the optimum doping profile and we discuss how the efficiency can be increased with that procedure. We find for Bi_2Te_3 that the gain of differential doping compared to uniform doping is about 13%.

Kurzfassung

Seit ihrer Entdeckung bieten thermoelektrische Materialien ein faszinierendes Forschungsfeld. Da sie eine einzigartige Möglichkeit darstellen Verlustwärme auf saubere und nachhaltige Weise in elektrische Energie zu konvertieren, können sie von großer Wichtigkeit für zukünftige Technologien sein. Gerade Materialien die sich gut für die Energieerzeugung eignen haben oft Transportkoeffizienten die stark von der Temperatur als auch von der Position des chemischen Potentials abhängen. Es existieren bereits einige Studien die auf die Temperaturabhängigkeit eingehen, aber keine die das chemische Potential auf der selben Ebene behandeln.

In dieser Arbeit lösen wir die makroskopischen Transportgleichungen wobei wir die Abhängigkeit der Transportkoeffizienten von Temperatur und chemischem Potential berücksichtigen. Wir diskutieren den Einfluss dieser erweiterten Behandlung auf die Effizienz thermoelektrischer Generatoren. Im Zuge dessen leiten wir adäquate Gleichungen und Randbedingungen für Kontakte zwischen zwei unterschiedlichen Materialien her.

Wir nutzen diese Gleichungen um ein thermoelektrisches Gerät mit zwei Zweigen zu beschreiben. Dabei gehen wir davon aus, dass zwei beliebige, aktive Materialien von zwei Metallen verbunden werden. Wir zeigen, dass die Gleichungen der zwei aktiven Regionen entkoppelt werden können, was die Komplexität stark reduziert. Um die verbleibenden nicht-linearen Differentialgleichungen zu lösen, erstellen wir eine Simulation die die Temperaturverteilung und das chemische Potential berechnet und im Anschluss daraus die Effizienz bestimmt. Da das Programm öffentlich gemacht werden soll, erstellen wir zusätzlich eine grafische Benutzeroberfläche. Wir präsentieren Simulationsergebnisse für Bi_2Te_3 , SrTiO_3 and FeSb_2 und vergleichen die berechneten Effizienzen mit Methoden die eine analytische Schätzung ermöglichen.

Wir stellen fest, dass das chemische Potential an den Kontakten weit entfernt von seinem Gleichgewichtswert liegen kann, was auf die Formation von Schottky Kontakten zurückzuführen ist und zu einer dramatischen Reduktion der Effizienz führen kann. Dieser Effekt ist im Feld der thermoelektrischen Materialien in der Vergangenheit vernachlässigt worden wodurch möglicherweise vielversprechende Materialien verworfen worden sind.

Zusätzlich erstellen wir eine numerische Routine die es erlaubt, das optimale Dotierungsprofil zu berechnen. Wir finden, dass die Effizienz von Bi_2Te_3 durch nicht-uniforme Dotierung um 13% höher ausfällt als mit uniformer.

Contents

| | |
|--|-----------|
| 1. Introduction | 6 |
| 2. Theory | 8 |
| 2.1. Basic relations and assumptions | 8 |
| 2.2. Efficiency and figure of merit | 11 |
| 2.3. Figure of merit for non-constant transport coefficients | 15 |
| 3. Thermoelectric transport equations and their solution | 17 |
| 3.1. Equations used | 17 |
| 3.2. Boundary conditions at junctions | 19 |
| 3.3. Summary of the equations | 22 |
| 3.4. Analytically solvable examples | 22 |
| 4. Simulation of the full thermoelement | 32 |
| 4.1. Model and equations | 32 |
| 4.2. Numerical implementation | 39 |
| 4.3. Optimization of the chemical potential position | 44 |
| 5. Results and interpretation | 46 |
| 5.1. Bi_2Te_3 | 46 |
| 5.1.1. Optimization | 49 |
| 5.2. SrTiO_3 | 52 |
| 5.3. FeSb_2 | 58 |
| 6. Conclusion | 60 |
| A. Program | 61 |
| A.1. Starting a simulation | 64 |
| A.2. Optimization routine | 64 |
| Bibliography | 66 |

1. Introduction

Thermoelectric materials have been a fascinating field of research ever since their first exploration. In 1821 Johann Thomas Seebeck discovered that a magnetic field was generated when he applied a temperature difference to the junctions of a closed loop of different materials [1]. Later it was found that the reason for this magnetic field was an electrical current which flows if two materials with different so-called Seebeck coefficients are connected and exposed to a temperature gradient. In a simple picture one can understand this phenomenon with charge carriers that diffuse from the hot side to the cold one and therefore generate an electrical current. However, in a real solid with a band-structure and interaction between the electrons and the lattice a more sophisticated theory has to be applied.

The reverse version of the Seebeck effect is called Peltier effect and was discovered in 1834 by Jean Charles Athanase Peltier [1]. He found that a junction of two materials can be cooled or heated when an electrical current is driven through it in one or the other direction.

The Seebeck and the Peltier effect give access to thermoelectric means of transforming heat into electrical power or using electrical currents for cooling purposes. In the past thermoelectric generators were only used in niche sectors as their efficiency is low compared to conventional heat converting machines. The largest advantage of thermoelectric generators lies in their reliability. Since they only consist of two blocks of different materials there are no moving parts which can break down or cause other dysfunctions. As long as a heat source supplies the generator with thermal energy the conversion into electrical power is ensured. This has been used to build so-called radioisotope thermoelectric generators (RTG) where the heat produced by the decay of a radioactive material is transformed into electrical power by a thermoelement [2]. These RTGs have been used for satellites and space probes like the Voyager 1 and 2. Further advantages of thermoelectric generators are the absence of exhaust gases and their longevity.

In recent years more and more efficient materials which show efficiencies of over 10% have been discovered which brought thermoelectric generators back into the focus as a real alternative to currently used electrical power generators [1, 3]. In order to further increase the performance it is necessary to get a better understanding of the complex interplay of different effects and mechanisms within the materials and the thermoelectric device as a whole.

Mahan has already discussed the case of variable chemical potentials for devices with constant transport coefficients [4, 5]. He has pointed out that the assumption

of a constant chemical potential causes a violation of the Poisson equation and solved the equations analytically for some special cases. He found that the efficiency of a thermoelectric generator is not affected by the variation of the chemical potential. In the case of constant transport coefficients the efficiency associated with the figure of Merit gives the correct value and is exact.

However, novel materials like FeSb_2 [6, 7] have been discovered for which the argument of constant transport coefficients is not a good approximation since they show a strong variation of their transport properties upon variations of the chemical potential.

In order to estimate the efficiency of devices consisting of such materials several strategies have been followed. One is the so-called averaged figure of Merit where the figure of Merit at different positions is averaged and the efficiency is calculated subsequently. This method has proven to give wrong results in some cases and contains theoretical inconsistencies. For this reason Kim et al. have introduced the so-called engineering figure of Merit recently [8]. They make the assumption of a linear temperature slope and that the chemical potential is at its equilibrium value but they include the dependence of the transport coefficients on the temperature and the chemical potential in an exact way.

All these previous studies have neglected the junctions between the materials since they assumed the thermal equilibrium chemical potential at every position within the materials. This, however violates the transport equations in a similar way as neglecting the chemical potential variations within the bulk violates the Poisson equation. The chemical potential can be far off its equilibrium value at the junction since it is influenced by the attached material. As a consequence the transport properties can change dramatically in a region around the junction and in turn strongly affect the efficiency. Therefore, in order to calculate the efficiency correctly even in materials with strongly position dependent chemical potential we include the junctions and the variable transport coefficients in our simulation. We calculate the spatial chemical potential- and temperature-distributions and subsequently the efficiency.

Furthermore we discuss the effect of differential doping on the efficiency. For that purpose we have developed a routine which calculates the optimal doping profile within a given material. This may open a new field for optimization and a further increase in efficiency.

2. Theory

2.1. Basic relations and assumptions

From equilibrium thermodynamics we know that we can assign a temperature T and a chemical potential μ to a volume which may exchange heat and particles with its surroundings. In non-equilibrium thermodynamics we have to account for temperature and chemical potential gradients and therefore we have to define what is meant by a position dependent T or μ as it is not so obvious from the theoretical point of view. To understand this we divide our actual system into small subsystems of finite volume V_i which have to be microscopically large so that they still contain many particles and a statistical description is justified (figure 2.1). We assume that the temperature and chemical potential and any other macroscopic quantities are constant within the volumes V_i . In the limit of macroscopically small subsystems (i.e. $V_i \ll V$) we can assign position dependent quantities

$$\mu \rightarrow \mu(\mathbf{r}) \quad (2.1)$$

$$T \rightarrow T(\mathbf{r}) \quad (2.2)$$

which perfectly coincides with our every day experience of locally different temperatures. Within each subsystem V_i as given in figure 2.1 we can set up the basic equation for the energy-density change at constant volume which reads

$$du = Tds + \mu dn + \phi d\rho . \quad (2.3)$$

This equations states that the total energy-density change ($d\mu$) is equal to the heat energy-density change (Tds) plus the potential energy-density change ($\mu dn + \phi d\rho$). The explicit position dependence of T , μ and ϕ is suppressed to improve the readability of the equations. As the ions are taken to be fixed on their lattice positions the particle number and charge variation stems from the electrons only. Therefore we can write

$$du = Tds + \mu dn + \phi d\rho = Tds + \mu dn + \phi(-e)dn = Tds - e \left(\phi - \frac{\mu}{e} \right) dn \quad (2.4)$$

which gives rise to the definition of the so-called electrochemical potential

$$\bar{\phi} \equiv \phi - \frac{\mu}{e} \quad (2.5)$$

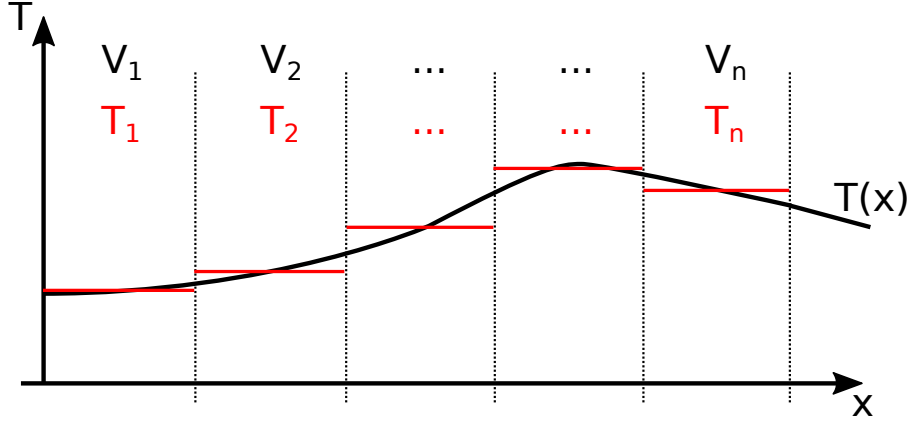


Figure 2.1.: Schematic picture showing the splitting into n subsystems. Each subsystem with volume V_i has its own temperature T_i . In the limit of large n we get a continuous temperature distribution $T(x)$. Note that each subsystem has to be in local thermal equilibrium and contains many particles so that the macroscopic quantities T and μ are well defined.

where e is the absolute value of the electron charge. By inserting this definition into equation (2.4) one obtains the compact expression

$$du = Tds + \bar{\phi}d\rho . \quad (2.6)$$

Note that the first term on the right-hand side represents the heat content of the total system (i.e. of the electrons and the ions) whereas the second term only depends on the electrons and can be seen as the change of the potential energy.

As the total energy and the charge have to be conserved we can write down continuity equations for the currents associated with these quantities which read

$$\frac{\partial u}{\partial t} + \nabla \cdot \mathbf{j}_u = 0 , \quad (2.7)$$

$$\frac{\partial \rho}{\partial t} + \nabla \cdot \mathbf{j} = 0 . \quad (2.8)$$

In this work we only discuss stationary systems which means that all time derivatives are zero and therefore

$$\nabla \cdot \mathbf{j}_u = 0 , \quad (2.9)$$

$$\nabla \cdot \mathbf{j} = 0 . \quad (2.10)$$

Instead of using the total energy current-density it is often more convenient and intuitive to use the heat current which is defined as

$$\mathbf{j}_Q \equiv \mathbf{j}_u - \bar{\phi}\mathbf{j} . \quad (2.11)$$

Note that although the divergence of \mathbf{j}_u and \mathbf{j} is zero in the stationary state the divergence of \mathbf{j}_Q will not be zero in general and therefore the heat is not a conserved quantity. The combination of the equations (2.9), (2.10) and (2.11) gives the relation

$$\nabla \cdot \mathbf{j}_u = 0 = \nabla \cdot \mathbf{j}_Q + \nabla \bar{\phi} \cdot \mathbf{j} \quad (2.12)$$

which we will need later.

At the beginning we have started from the assumption that the temperature and electrochemical potential gradients are small enough that a local thermal equilibrium can be established. Following this requirement of relatively slowly changing fields it makes sense to use transport equations which are linearized with respect to those fields, i.e.

$$\mathbf{j} = -\sigma \nabla \bar{\phi} - \sigma \alpha \nabla T, \quad (2.13)$$

$$\mathbf{j}_Q = -\sigma \alpha T \nabla \bar{\phi} - (\kappa + \sigma \alpha^2 T) \nabla T. \quad (2.14)$$

which are the well-known linear transport equations. The reason for the fact that only three independent transport coefficients occur lies in the microscopical time-reversibility of physical processes and is known as Onsager's reciprocal relations [9, 10] which we will not discuss here. The transport coefficients are called electrical conductivity (σ), the Seebeck coefficient (α) and the thermal conductivity (κ) which may depend on the temperature and the chemical potential,

$$\sigma \rightarrow \sigma(\mu, T), \alpha \rightarrow \alpha(\mu, T), \kappa \rightarrow \kappa(\mu, T). \quad (2.15)$$

For convenience the explicit dependence will be dropped from now on. Note that in general the transport coefficients are tensors but in this work we will treat them as scalars as we are not interested in anisotropic effects. With equation (2.13) we can eliminate the electrochemical potential gradient in equation (2.14) to get a more convenient version of the transport equations,

$$\mathbf{j} = -\sigma \nabla \bar{\phi} - \sigma \alpha \nabla T, \quad (2.16)$$

$$\mathbf{j}_Q = \alpha T \mathbf{j} - \kappa \nabla T. \quad (2.17)$$

The equation (2.16) states that the driving force of an electrical current at constant temperature is not only the electrical field but an effective field calculated from the electrochemical potential. However in metals the chemical potential μ is almost constant which is the reason why most people are more used to the simple form $j = \sigma \mathbf{E}$.

When we insert equation (2.17) into equation (2.12) and exploit the vanishing of the electrical current divergence we get the so-called Domenicali equation [11] which reads

$$\frac{\mathbf{j}^2}{\sigma} + \nabla \cdot (\kappa \nabla T) - T \mathbf{j} \cdot \nabla \alpha = 0 \quad (2.18)$$

and represents the local energy conservation. The first term is the well-known irreversible Joule heating, the second term accounts for a changing thermal conductivity and the third one is the reversible Thomson heating [12].

2.2. Efficiency and figure of merit

One field of applications for thermoelectric materials is power generation. In that case two pieces of different materials are brought into thermal contact with heat reservoirs at different temperatures (figure 2.2). Due to the Seebeck effect an elec-

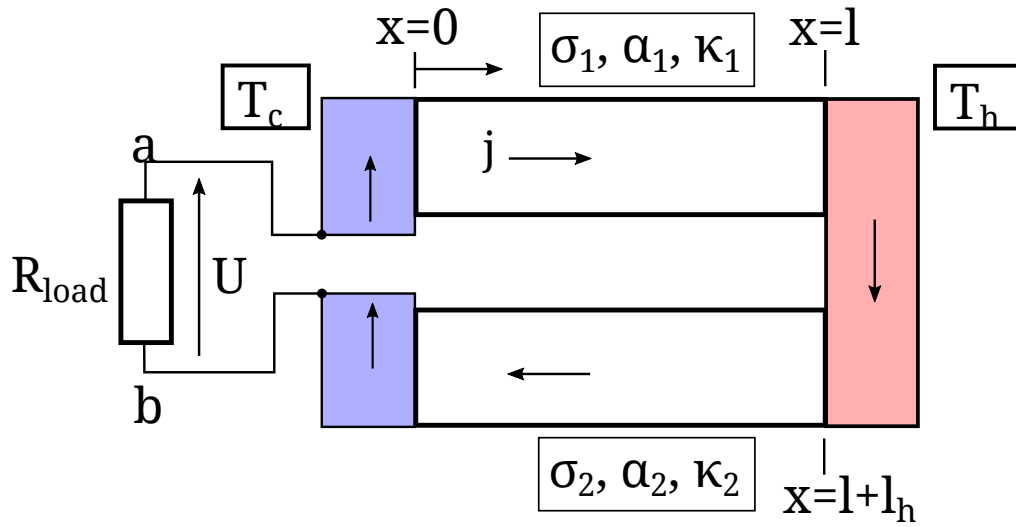


Figure 2.2.: Schematic picture showing a power generator with two legs consisting of different thermoelectric materials. The blue and red areas are metals held at constant temperatures T_c and T_h ($T_h > T_c$). They are assumed to be ideal conductors which means zero electrical resistance.

trochemical potential gradient is established and an electrical current flows through the attached load. In this section we are going to introduce the so-called figure of merit for a device with constant transport coefficients. For the following theoretical treatment we additionally assume that all metals (i.e. the blue and red areas and the wires which connect the load with the generator in figure 2.2) have zero electrical resistance. This simplification is only used in this section and not in the final simulation as discussed in section 4.1.

When we want to use generators the two most important quantities to classify them are the output power and the efficiency. The power is defined as

$$P = \Delta\bar{\phi}I \quad (2.19)$$

where I denotes the electrical current. We have used the electrochemical potential drop $\Delta\bar{\phi}$ at the load as it represents the change in the potential energy of the electrons rather than the electrical potential only. In metals the chemical potential is almost constant which is the reason why one usually only takes into account the electrical voltage $U = \Delta\phi$ for power calculations. We can calculate $\Delta\bar{\phi}$ by expressing $\bar{\phi}'$ with equation (2.16) and integrating from one side of the load to the other one along the thermoelectric device,

$$\Delta\bar{\phi} = \int_a^b dx \bar{\phi}' = \int_a^b dx \left(-\frac{j(x)}{\sigma(x)} - \alpha(x)T'(x) \right). \quad (2.20)$$

Using the definitions for the electrical resistance $R = \frac{l}{\sigma A}$ and the electrical current $I = Aj$ where A denotes the cross-sectional area and l the length of the thermoelectric leg we get

$$\Delta\bar{\phi} = (\alpha_2 - \alpha_1)(T_h - T_c) - (R_1 + R_2)I \equiv \alpha\Delta T - RI \quad (2.21)$$

and eventually the power reads

$$P = (\alpha\Delta T - RI)I. \quad (2.22)$$

In this equation we have introduced new coefficients $\alpha = \alpha_2 - \alpha_1$ and $R = R_1 + R_2$ which represent the whole thermoelectric device. According to equation (2.22) the power that is delivered to the load depends on the current which itself depends implicitly on the resistance of the load R_{load} . We can find the optimum current by differentiation of the power $\frac{\partial P}{\partial I}(I_m) = 0$ which gives

$$I_m = \frac{\alpha\Delta T}{2R} \quad (2.23)$$

and with Ohm's law we can determine the value of the load resistance that has to be attached in order to achieve the optimum current,

$$R_{\text{load-m}} = \frac{\Delta\bar{\phi}(I_m)}{I_m} = R. \quad (2.24)$$

This means that the maximum power is delivered to the load when its resistance matches the internal resistance of the source.

The so-called efficiency of a thermoelectric generator is defined as

$$\eta \equiv \frac{P}{I_Q(T_h)} \quad (2.25)$$

where P stands for the power as discussed above and I_Q is the total heat current which enters the generator from the hot side. In terms of heat current densities we can write

$$I_Q \equiv A(j_Q(l + l_h) - j_Q(l)) = (\alpha_2 - \alpha_1)T_h I - A(\kappa_2 T'(l + l_h) - \kappa_1 T'(l)) \quad (2.26)$$

where the different signs between $j_Q(l + l_h)$ and $j_Q(l)$ assure that heat flowing from the hot side into the device is counted positive. With the Domenicali equation (2.18) we can calculate the temperature distribution and then get rid of the temperature derivatives in equation (2.26) which gives

$$I_Q = \alpha T_h I + \frac{A}{l}(\kappa_1 + \kappa_2)\Delta T - RI^2/2 \quad (2.27)$$

where we have assumed that both legs of the generator have the same length and cross-sectional areas for simplicity. With the definition of the efficiency (2.25) and the relation for the output power (2.22) we eventually get

$$\eta = \frac{(\alpha\Delta T - RI) I}{\alpha T_h I + \frac{A}{l}(\kappa_1 + \kappa_2)\Delta T - RI^2/2} . \quad (2.28)$$

The efficiency can be optimized with respect to the electrical current in the same way as the output power which gives the famous formula

$$\eta_m = \frac{T_h - T_c}{T_h} \frac{\sqrt{1 + ZT_m} - 1}{\sqrt{1 + ZT_m} + T_c/T_h} \quad (2.29)$$

with the mean temperature $T_m \equiv (T_h + T_c)/2$ and the so-called figure of merit for a two-leg thermoelectric generator,

$$Z \equiv \frac{(\alpha_2 - \alpha_1)^2}{(\kappa_1 + \kappa_2)(\frac{1}{\sigma_1} + \frac{1}{\sigma_2})} . \quad (2.30)$$

The first term on the right-hand side of equation (2.29) is the Carnot efficiency which is the maximum that can be achieved by a generator operating between the temperatures T_h and T_c . The load resistance for which the generator shows the efficiency (2.29) can be derived as

$$R_{\text{load-m}} = R\sqrt{1 + ZT_m} . \quad (2.31)$$

The figure of merit is often used to classify thermoelectric materials as it corresponds to the maximum efficiency. In the limit of $Z \rightarrow \infty$ the efficiency of the device becomes the Carnot efficiency whereas in case of $Z = 0$ the efficiency becomes zero. Note that the relations given above incorporate the single-leg relations which can be obtained by setting $\alpha_2 = 0$, $\sigma_2 \rightarrow \infty$ and $\kappa_2 = 0$. This gives the single-leg figure of merit which reads

$$Z_{\text{single}} = \frac{\alpha_1^2 \sigma_1}{\kappa_1} . \quad (2.32)$$

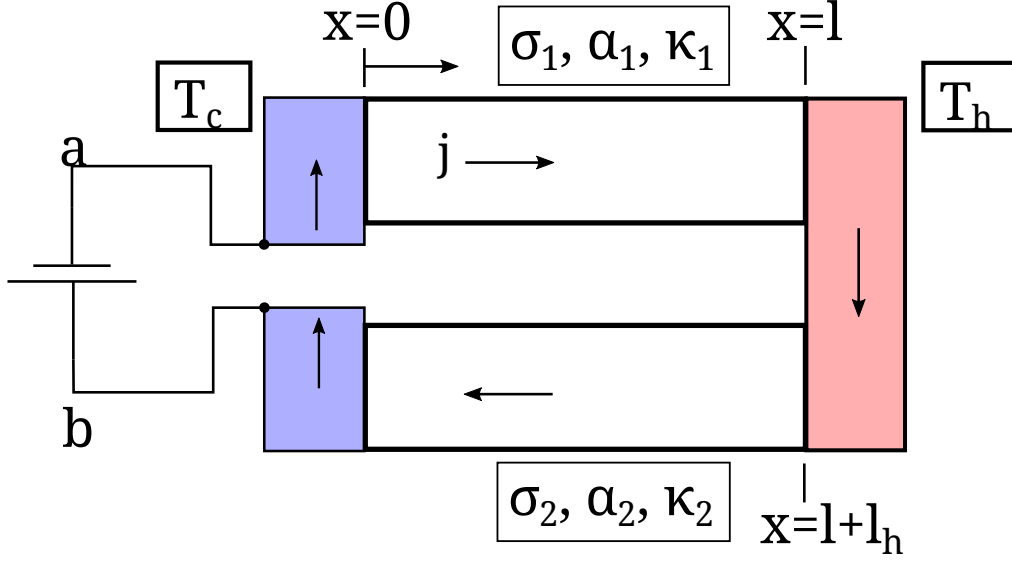


Figure 2.3.: Schematic picture showing a thermoelectric cooler with two legs consisting of different materials and a battery which drives the electrical current. The blue and red areas are metals held at constant temperatures T_c and T_h ($T_h > T_c$).

When the load resistor R_{load} in figure 2.2 is replaced by a battery which drives the electrical current in the opposite direction the thermoelectric device can work as a refrigerator. In that case the efficiency is defined as

$$\eta_{\text{cool}} \equiv \frac{I_Q(T_c)}{-\Delta\bar{\phi}I} \quad (2.33)$$

which is the heat per second taken from the cold side divided by the power that is supplied by the battery (figure 2.3). The minus sign in the denominator accounts for the reversed current direction and ensures that the efficiency is positive in case of cooling. In a similar way as above one can show [9] that the efficiency at a given current I reads

$$\eta_{\text{cool}} = \frac{-\alpha T_c I - \frac{A}{l}(\kappa_1 + \kappa_2) - RI^2/2}{-\alpha \Delta T + RI^2} \quad (2.34)$$

and in total analogy the maximum efficiency is

$$\eta_{\text{cool-m}} = \frac{T_c}{T_h - T_c} \frac{\sqrt{1 + ZT_m} - T_h/T_c}{\sqrt{1 + ZT_m} + 1}. \quad (2.35)$$

2.3. Figure of merit for non-constant transport coefficients

The figure of merit as introduced in section 2.2 is a suitable quantity for materials with transport coefficients that are independent of the temperature and the chemical potential. However, many materials which show large Seebeck coefficients are semiconductors and therefore have transport properties that may vary strongly. In order to simply estimate the efficiency of a material with non-constant coefficients two different ways have been used in the past as pointed out in [8]. The idea behind both variants is to calculate a new figure of merit that accounts for the variation of the transport coefficients and use equation (2.29) to determine the efficiency.

The first one is the actual figure of merit taken at the mean temperature $T_m = (T_h + T_c)/2$,

$$Z_{\text{avg-i}} \equiv \frac{\alpha(T_m)^2 \sigma(T_m)}{\kappa(T_m)} \quad (2.36)$$

and the second one is to really average the figure of merit over the temperature range, i.e.

$$Z_{\text{avg-ii}} \equiv \frac{1}{T_h - T_c} \int_{T_c}^{T_h} dT \frac{\alpha(T)^2 \sigma(T)}{\kappa(T)}. \quad (2.37)$$

Although these methods have been commonly used they do not give very good results for strongly varying coefficients. Additionally there is the theoretical inconsistency that the maximum efficiency given by equation 2.2 is only valid for the optimal output current. When the material has locally different values for the figure of merit, the optimal current would be different at each position as it depends on the transport coefficients as well. However, the electrical current is constant throughout the device which means that there is a fundamental contradiction. This has been recognized by [8] who introduced the so-called engineering figure of merit that gives much more realistic values for the efficiency.

The engineering figure of merit is defined as

$$(ZT)_{\text{eng}} \equiv \frac{\left(\int_{T_c}^{T_h} dT \alpha(T) \right)^2}{\int_{T_c}^{T_h} dT \frac{1}{\sigma(T)} \int_{T_c}^{T_h} dT \kappa(T)} \quad (2.38)$$

and the maximum efficiency is given as

$$\eta_{\text{eng-m}} = \eta_c \frac{\sqrt{1 + (ZT)_{\text{eng}} \alpha_1 \eta_c^{-1}} - 1}{\alpha_0 \sqrt{1 + (ZT)_{\text{eng}} \alpha_1 \eta_c^{-1}} + \alpha_2} \quad (2.39)$$

with the Carnot efficiency $\eta_c = (T_h - T_c)/T_h$. The coefficients α_i are defined as

$$\alpha_i = \frac{\alpha(T_h) \Delta T}{\int_{T_c}^{T_h} dT \alpha(T)} - \frac{\int_{T_c}^{T_h} dT T \frac{d\alpha(T)}{dT}}{\int_{T_c}^{T_h} dT \alpha(T)} W_T \eta_c - i W_J \eta_c \quad (2.40)$$

with

$$W_T = \frac{\int_{T_c}^{T_h} dT \int_T^{T_h} d\tilde{T} \left(\tilde{T} \frac{d\alpha(\tilde{T})}{d\tilde{T}} \right)}{\Delta T \int_{T_c}^{T_h} dT \left(T \frac{d\alpha(T)}{dT} \right)} \text{ and } W_J = \frac{\int_{T_c}^{T_h} dT \int_T^{T_h} d\tilde{T} \frac{1}{\sigma(\tilde{T})}}{\Delta T \int_{T_c}^{T_h} dT \frac{1}{\sigma(T)}} . \quad (2.41)$$

Although the engineering figure of merit and the formulas given for the maximum efficiency may look complicated on the first sight they can be easily calculated by means of numerical integration. The transport coefficients used above are evaluated at the equilibrium chemical potential corresponding to the local temperature which means

$$\alpha(T) \equiv \alpha(\mu_{eq}(T), T) , \sigma(T) \equiv \sigma(\mu_{eq}(T), T) , \kappa(T) \equiv \kappa(\mu_{eq}(T), T) \quad (2.42)$$

and the temperature distribution between the heat reservoirs is assumed to be a linear slope. This is of course a severe simplification that can lead to significant differences compared to the full simulation especially for materials with transport properties strongly dependent on temperature and chemical potential.

3. Thermoelectric transport equations and their solution

3.1. Equations used

As pointed out in chapter 1 we seek to calculate the chemical potential and temperature distribution $(\mu(x), T(x))$ for a thermoelectric device with two legs (see figure 2.2). Once we have these quantities we can easily determine the output power and the efficiency or the cooling efficiency respectively. For simplicity we will assume that all quantities only depend on one spatial dimension (x) which would correspond to a device with constant cross-sectional areas that are large compared to the length of the device. This is a good assumption as long as surface effects can be neglected.

The first equation that is needed is equation (2.16) which (in one dimension) reads

$$j(x) = - \underbrace{\sigma(x, \mu(x), T(x))}_{\sigma(x)} \left(\underbrace{\left(\phi'(x) - \frac{1}{e} \mu'(x) \right)}_{\bar{\phi}'(x)} + \underbrace{\alpha(x, \mu(x), T(x))}_{\alpha(x)} T'(x) \right) \quad (3.1)$$

where we have taken into account that all transport coefficients depend on the position via their dependence on $\mu(x)$ and $T(x)$ as well as explicitly which represents regions of different materials. The current density fulfills a continuity equation as the charge is a conserved quantity, i.e.

$$\frac{dQ}{dt} = - \oint_{\partial V} d\mathbf{f} \cdot \mathbf{j}(\mathbf{x}) . \quad (3.2)$$

In our one dimensional case with constant cross-sectional areas this relation gives for the steady state

$$j(x_1) = j(x_2) \quad \forall x_1, x_2 \quad (3.3)$$

which means that the current density is constant throughout the whole device. The current density in equation (3.1) will be treated as an input parameter which is equivalent to specifying the load resistance R_{load} or the electrochemical potential

drop $\Delta\bar{\phi}$ at the load. Once we have solved the problem we can determine $\Delta\bar{\phi}$ corresponding to the given j by integrating equation (3.1) and subsequently calculate the load resistance with Ohm's law. Now that we have identified j as input there are three independent variables left which are the chemical potential $\mu(x)$, the electrical potential $\phi(x)$ and the temperature $T(x)$. To solve the system we therefore need two further equations.

The first one is the so-called Domenicali equation (see chapter 2.1) which can be derived from energy conservation (equation (2.9)),

$$\frac{j^2}{\sigma(x)} + \kappa'(x)T'(x) + \kappa(x)T''(x) - T(x)j\alpha'(x) = 0 . \quad (3.4)$$

The second additional equation we need has to account for the fact that the electrical charge and the electrical field are not independent but connected by Maxwell's equations. As we completely neglect magnetic fields and we are only interested in the steady state we need Gauß's law in matter,

$$\oint_{\partial V} \mathbf{df} \cdot \mathbf{D}(\mathbf{x}) = \int_V d^3x \rho_f(\mathbf{x}) \quad (3.5)$$

where \mathbf{D} is the displacement field used in macroscopic electrodynamics. The corresponding "free" charge density ρ_f is the charge accumulation due to the possible non-equilibrium position of the chemical potential. Within a region consisting of one type of material the displacement field and the electrical field are connected by the relation

$$\mathbf{D} = \epsilon_0 \epsilon \mathbf{E} \quad (3.6)$$

with ϵ , the relative permittivity that is assumed to be constant and ϵ_0 , the vacuum permittivity. The differential version of equation (3.5) is called Poisson's equation and for the one dimensional case reads

$$E'(x) = \frac{\rho_f(x)}{\epsilon_0 \epsilon} = -\phi''(x) \quad (3.7)$$

where we have used the definition of the electrical potential.

Summarizing, we have the three equations

$$\frac{j^2}{\sigma} + \kappa' T' + \kappa T'' - T j \alpha' = 0 , \quad (3.8a)$$

$$j = -\sigma \left(\phi' - \frac{1}{e} \mu' \right) - \sigma \alpha T' , \quad (3.8b)$$

$$\phi'' = -\frac{\rho_f}{\epsilon_0 \epsilon} \quad (3.8c)$$

where we have dropped the dependence on the position for better readability. The equations given above are three coupled, nonlinear differential equations which are difficult to solve even numerically. A more convenient set of equations can be obtained by differentiating equation (3.8b), taking into account that $j' = 0$ and then substituting ϕ'' according to equation (3.8c) which gives

$$-\frac{1}{e}\mu'' = \frac{\rho_f}{\epsilon_0\epsilon} + \frac{j}{\sigma^2}\sigma' - \alpha'T' - \alpha T'' . \quad (3.9)$$

The main advantage of this formulation is that the electrical potential has completely vanished which leaves us with only two coupled differential equations in two variables, namely $T(x)$ and $\mu(x)$. In the end the electrical potential can be recovered with equation (3.8c) if needed.

By applying Gauß's law in the differential form with constant permittivity we have restricted the use of the equation to a region consisting of one type of material. As we want to describe a device consisting of several different regions we have to find proper boundary conditions to combine the solutions.

3.2. Boundary conditions at junctions

In this section we will derive the boundary conditions that are needed to combine the solutions of regions with different materials according to physical laws (see figure 3.1). At first we will have a look at the behavior of the free charge density ρ_f at the

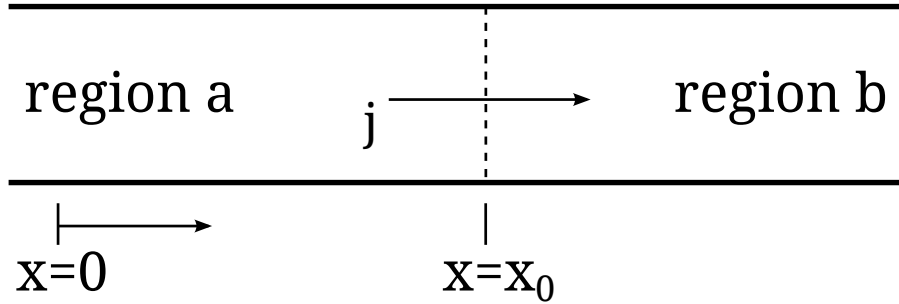


Figure 3.1.: Schematic picture of an interface between two regions a and b of different materials.

interface $x = x_0$. As discussed above the free charge density accounts for the local charge accumulation due to a non-equilibrium chemical potential. We explicitly describe the spatial electron distribution via $\mu(x)$ and therefore, by construction, there must not be an additional infinitesimal free surface charge layer. This means that the charge density may be discontinuous at the interface but it does not contain δ -distribution-like terms. Therefore we can apply Gauß's law in the form (3.5) and

integrate over a small volume including the interface. In the limit of an infinitesimal integration volume this gives the relation

$$D(x_0^-) = D(x_0^+) \quad (3.10)$$

which means that the displacement field is continuous in case of vanishing free surface charges. Together with equation (3.6) this gives

$$\epsilon_a \phi'(x_0^-) = \epsilon_b \phi'(x_0^+) \quad (3.11)$$

which indicates the jump of the electrical field due to polarization surface charges. The electrical potential itself is, by construction, continuous which means

$$\phi(x_0^-) = \phi(x_0^+) . \quad (3.12)$$

From equation (3.8b) we can express the electrochemical potential derivative,

$$\bar{\phi}'(x) = -\frac{j}{\sigma(x)} - \alpha(x)T'(x) \quad (3.13)$$

which we integrate over a small region around x_0 in order to find the behavior of $\bar{\phi}$ at the interface,

$$\bar{\phi}(x_0 + \Delta) - \bar{\phi}(x_0 - \Delta) = - \int_{x_0 - \Delta}^{x_0 + \Delta} dx \left(\frac{j}{\sigma(x)} + \alpha(x)T'(x) \right) . \quad (3.14)$$

The first term within the integral is the (constant) current density divided by the the electrical conductivity which may be discontinuous at x_0 but must not contain terms $\propto \delta(x - x_0)$ for obvious reasons. The same holds for the Seebeck coefficient and the temperature derivative as the temperature must be continuous according to the laws of thermodynamics. Hence, we find in the limit $\Delta \rightarrow 0$ that the electrochemical potential is continuous

$$\bar{\phi}(x_0^+) - \bar{\phi}(x_0^-) = 0 \quad (3.15)$$

and with equation (3.12) and the definition of the electrochemical potential we find the same for the chemical potential subsequently

$$\mu(x_0^+) - \mu(x_0^-) = 0 . \quad (3.16)$$

The fact that ϕ , $\bar{\phi}$ and μ are continuous is not surprising as they are potential energies and a discontinuous jump would lead to infinite forces which would be unphysical in this context.

As we are going to deal with two second-order differential equations, namely for T and μ we have to determine relations for the first derivatives of these quantities

at the interface. We can exploit equation (3.8b) to express the electrochemical potential derivative, evaluate it on both sides of the interface and then build the difference which gives

$$\bar{\phi}'(x_0^+) - \bar{\phi}'(x_0^-) = -j \left(\frac{1}{\sigma(x_0^+)} - \frac{1}{\sigma(x_0^-)} \right) - \alpha(x_0^+)T'(x_0^+) + \alpha(x_0^-)T'(x_0^-) . \quad (3.17)$$

However, we are going to work with μ rather than with $\bar{\phi}$ which is the reason why we would like to know the behavior of μ' as well. Therefore we calculate the first derivative change of the electrical potential at the interface,

$$\phi'(x_0^+) - \phi'(x_0^-) = \phi'(x_0^-) \left(\frac{\epsilon_a}{\epsilon_b} - 1 \right) \quad (3.18)$$

where we have employed equation (3.11). We can get rid of the electrical potential on the right hand side with equation (3.8b) which gives

$$\phi'(x_0^+) - \phi'(x_0^-) = \left(\frac{\epsilon_a}{\epsilon_b} - 1 \right) \left(-\frac{j}{\sigma(x_0^-)} + \frac{1}{e} \mu'(x_0^-) - \alpha(x_0^-)T'(x_0^-) \right) . \quad (3.19)$$

When we insert equation (3.19) into (3.17) we completely get rid of ϕ' which leaves a relation for the chemical potential that reads

$$\frac{\epsilon_b}{e} \mu'(x_0^+) - \frac{\epsilon_a}{e} \mu'(x_0^-) = j \left(\frac{\epsilon_b}{\sigma(x_0^+)} - \frac{\epsilon_a}{\sigma(x_0^-)} \right) + \epsilon_b \alpha(x_0^+)T'(x_0^+) - \epsilon_a \alpha(x_0^-)T'(x_0^-) . \quad (3.20)$$

We now have calculated all necessary relations for the chemical potential, what is left is a set of boundary conditions for the temperature. As mentioned above the temperature itself has to be continuous according to fundamental thermodynamics, i.e.

$$T(x_0^+) - T(x_0^-) = 0 . \quad (3.21)$$

If we want to describe a junction between two different materials we in principle need a relation for the first derivative of the temperature, too, as the Domenicali equation is second order. However, this is only needed in case of a conserved total energy current j_u which is not the case when the junction is artificially held at constant temperature on one side. For a two-leg thermoelectric device only such junctions are present but for the sake of completeness we give the relation for the temperature derivative as well. This can be obtained by exploiting the fact that the total energy current is conserved,

$$j_u(x_0^+) - j_u(x_0^-) = 0 \quad (3.22)$$

and with the equations (2.11), (2.17), (3.21) and (3.15) we obtain

$$\kappa(x_0^+)T'(x_0^+) - \kappa(x_0^-)T'(x_0^-) = jT(x_0) (\alpha(x_0^+) - \alpha(x_0^-)) . \quad (3.23)$$

3.3. Summary of the equations

In total we have two second-order, coupled differential equations for the temperature and the chemical potential which read

$$\frac{j^2}{\sigma} + \kappa' T' + \kappa T'' - T j \alpha' = 0 , \quad (3.24a)$$

$$-\frac{1}{e} \mu'' = \frac{\rho_f}{\epsilon_0 \epsilon} + \frac{j}{\sigma^2} \sigma' - \alpha' T' - \alpha T'' \quad (3.24b)$$

where all transport coefficients and ρ may depend on the $\mu(x)$ and $T(x)$ and on x explicitly,

$$\rho = \rho(x, \mu, T) , \sigma = \sigma(x, \mu, T) , \alpha = \alpha(x, \mu, T) , \kappa = \kappa(x, \mu, T) . \quad (3.25)$$

Note that equation (3.24a) only holds within a region where the total energy current is conserved whereas equation (3.24b) can be applied to every region where the electrical current is conserved i.e. the whole device. Furthermore we have derived boundary conditions for junctions (at $x = x_0$) between two different regions a and b which read

$$\mu(x_0^-) = \mu(x_0^+) , \quad (3.26a)$$

$$\frac{\epsilon_b}{e} \mu'(x_0^+) - \frac{\epsilon_a}{e} \mu'(x_0^-) = j \left(\frac{\epsilon_b}{\sigma(x_0^+)} - \frac{\epsilon_a}{\sigma(x_0^-)} \right) + \epsilon_b \alpha(x_0^+) T'(x_0^+) - \epsilon_a \alpha(x_0^-) T'(x_0^-) , \quad (3.26b)$$

$$T(x_0^-) = T(x_0^+) , \quad (3.26c)$$

$$\kappa(x_0^+) T'(x_0^+) - \kappa(x_0^-) T'(x_0^-) = j T(x_0) (\alpha(x_0^+) - \alpha(x_0^-)) . \quad (3.26d)$$

As the Domenicali equation itself the boundary condition (3.26d) only holds if the total energy current through the junction is conserved.

3.4. Analytically solvable examples

As mentioned in chapter 2.2 we can analytically determine the efficiency for the case of constant transport coefficients which is a function of the figure of merit $Z = \frac{\sigma \alpha^2}{\kappa}$. However it is instructive to solve the full set of equations given in chapter 3.3 for some model cases and calculate the μ -, T - and ϕ - distributions in order to get a feeling for the physics. As this work is partially based on a previous project thesis [13] written by myself there are parts of the following derivation that are the same as in that previous work.

At first we will discuss an infinitely long rod of material which is held at the temperature T_0 for $x < 0$ and T_l for $x > l$ respectively (see figure 3.2). We assume that there is an electrical current j flowing through the rod and as we neglect

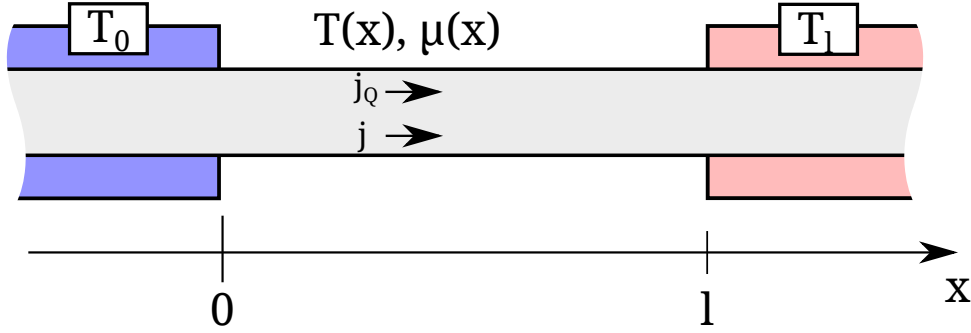


Figure 3.2.: Schematic picture of an infinitely long rod held at constant temperature T_0 for $x < 0$ and T_l for $x > l$ respectively.

the effects due to surfaces, j is a constant. As we know that the Seebeck effect generates a voltage when a temperature gradient is applied we would expect charge accumulations at $x = 0$ and $x = l$ which have opposite sign. We will see that this is indeed true but that things can become less intuitive in some cases.

Since we seek to solve the equations for μ and T we need a model for the charge density ρ_f . The charge density of a material which is not highly correlated can be written as

$$\rho_f(\mu, T) = -e \int d\epsilon N(\epsilon) f(\epsilon, \mu, T) + \rho_{\text{ION}} \quad (3.27)$$

where we have used the non-interacting density-of-states $N(\epsilon)$ and the Fermi-Dirac distribution f . In case of a metal the chemical potential lies in a region where $N(\epsilon)$ has a finite and usually high value which would mean that the charge density increases dramatically when increasing μ . This justifies the assumption that the chemical potential stays close to its equilibrium value in metals and hence, we can linearize ρ_f with respect to μ ,

$$\rho_f(\mu, T) = \underbrace{\rho_f(\mu_{\text{eq}}, T)}_{\equiv 0} + \frac{\partial \rho_f}{\partial \mu}(\mu_{\text{eq}}, T) (\mu - \mu_{\text{eq}}) + O((\mu - \mu_{\text{eq}})^2) \quad (3.28)$$

and with equation (3.27) we get

$$\rho_f(\mu, T) \approx -e(\mu - \mu_{\text{eq}}) \int d\epsilon N(\epsilon) \frac{\partial f}{\partial \mu}(\epsilon, \mu_{\text{eq}}, T) \approx -e(\mu - \mu_{\text{eq}}) N(\mu_{\text{eq}}). \quad (3.29)$$

In the last step we have assumed that the temperature is sufficiently low so that $N(\epsilon)$ changes only slightly within the interval $\mu_{\text{eq}} \pm k_B T$. With the same argument we can justify the assumption that the equilibrium chemical potential μ_{eq} is independent of the temperature. In order to simplify the readability we define

$$\xi^2 \equiv \frac{e^2 N(\mu_{\text{eq}})}{\epsilon_0} \quad (3.30)$$

where ϵ_0 denotes the permittivity of vacuum. With this definition the charge density for metals eventually reads

$$\rho_f(\mu) = -\frac{\epsilon_0 \xi^2}{e}(\mu - \mu_{\text{eq}}) . \quad (3.31)$$

With this simple relation we have enough information to solve the constant coefficient problem for the setup shown in figure 3.2. Summarizing we can say that the transport problem can be solved analytically when the transport coefficients are constants, the band-structure is independent of the number of particles and when the density-of-states can be assumed constant within the interval $\mu_{\text{eq}} \pm k_B T$.

We can express the second derivative of T for the region $0 \leq x \leq l$ with the Domenicali equation (3.24a) which gives

$$T''(x) = \begin{cases} 0 & x < 0 \\ -\frac{j^2}{\sigma\kappa} \equiv \frac{c}{\alpha} = \text{const.} & 0 \leq x \leq l \\ 0 & x > l \end{cases} \quad (3.32)$$

where we have introduced the new constant c . We can solve equation (3.32) by integrating it twice which gives

$$T(x) = \begin{cases} T_0 & x < 0 \\ -\frac{j^2}{2\sigma\kappa}(x^2 - lx) + \frac{T_l - T_0}{l}x + T_0 & 0 \leq x \leq l \\ T_l & x > l \end{cases} . \quad (3.33)$$

When we insert equation (3.31) into equation (3.24b) we can express the second derivative of the chemical potential as

$$\frac{1}{e}\mu''(x) = \begin{cases} \frac{\xi^2}{e}(\mu - \mu_{\text{eq}}) & x < 0 \\ \frac{\xi^2}{e}(\mu - \mu_{\text{eq}}) + c & 0 \leq x \leq l \\ \frac{\xi^2}{e}(\mu - \mu_{\text{eq}}) & x > l \end{cases} . \quad (3.34)$$

We can get rid of the $1/e$ factors by switching the unit of μ from Joule to Electronvolt which we do in the simulations. For the sake of generality we write them explicitly in this section. The solution of equation (3.34) can be obtained by substitution and integration which gives

$$\frac{1}{e}\mu = \begin{cases} a_1 e^{\xi x} + b_1 e^{-\xi x} + \frac{1}{e}\mu_{\text{eq}} & x < 0 \\ a_2 e^{\xi x} + b_2 e^{-\xi x} - \frac{c}{\xi^2} + \frac{1}{e}\mu_{\text{eq}} & 0 \leq x \leq l \\ a_3 e^{\xi x} + b_3 e^{-\xi x} + \frac{1}{e}\mu_{\text{eq}} & x > l \end{cases} . \quad (3.35)$$

The c is the same as defined by equation (3.32) while a_i and b_i are integration constants which still must be determined. Although it is true that the whole rod is made of the same material there are discontinuities in the total energy current at

the junctions $x = 0$ and $x = l$ due to the heat baths. This leads to discontinuities in the first derivatives of the temperature and in turn affects the chemical potential. Therefore we have to apply the boundary conditions (3.26a) and (3.26b) at the junctions as they correctly resemble this situation. Since we describe a metal we assume that the relative permittivity is one i.e. $\epsilon_{a/b} = 1$.

The boundary conditions (3.26b) then read

$$\mu(0^-) = \mu(0^+) , \quad (3.36a)$$

$$\mu(l^-) = \mu(l^+) , \quad (3.36b)$$

and with the temperature distribution (3.33) and (3.26b) we additionally get

$$\frac{1}{e}\mu'(0^+) - \frac{1}{e}\mu'(0^-) = \alpha(T'(0^+) - T'(0^-)) = \alpha\left(\frac{j^2 l}{2\sigma\kappa} + \frac{T_l - T_0}{l}\right) , \quad (3.37a)$$

$$\frac{1}{e}\mu'(l^+) - \frac{1}{e}\mu'(l^-) = \alpha(T'(l^+) - T'(l^-)) = \alpha\left(\frac{j^2 l}{2\sigma\kappa} - \frac{T_l - T_0}{l}\right) . \quad (3.37b)$$

Furthermore we know that the chemical potential has to stay finite for $x \rightarrow \pm\infty$ which gives another two conditions. Eventually we find for the constants

$$a_1 = \left(\frac{c}{2\xi^2} - b\right)(e^{-\xi l} - 1) + \frac{cl}{4\xi}(e^{-\xi l} + 1) \quad (3.38a)$$

$$b_1 = 0 \quad (3.38b)$$

$$a_2 = \left(\frac{c}{2\xi^2} + \frac{cl}{4\xi} - b\right)e^{-\xi l} \quad (3.38c)$$

$$b_2 = \frac{c}{2\xi^2} + \frac{cl}{4\xi} + b \quad (3.38d)$$

$$a_3 = 0 \quad (3.38e)$$

$$b_3 = \left(\frac{c}{2\xi^2} + b\right)(1 - e^{\xi l}) + \frac{cl}{4\xi}(e^{\xi l} + 1) \quad (3.38f)$$

with the factors c and b which are defined as

$$c \equiv -\frac{\alpha j^2}{\sigma\kappa} , \quad (3.39)$$

$$b \equiv -\frac{\alpha}{2\xi} \frac{Tl - T_0}{l} . \quad (3.40)$$

The results are shown in figures 3.3(a)-3.3(d). In this example the Seebeck coefficient is negative which represents a material which excess electrons if the Seebeck coefficient stems from an electron hole asymmetry and not from other effects like

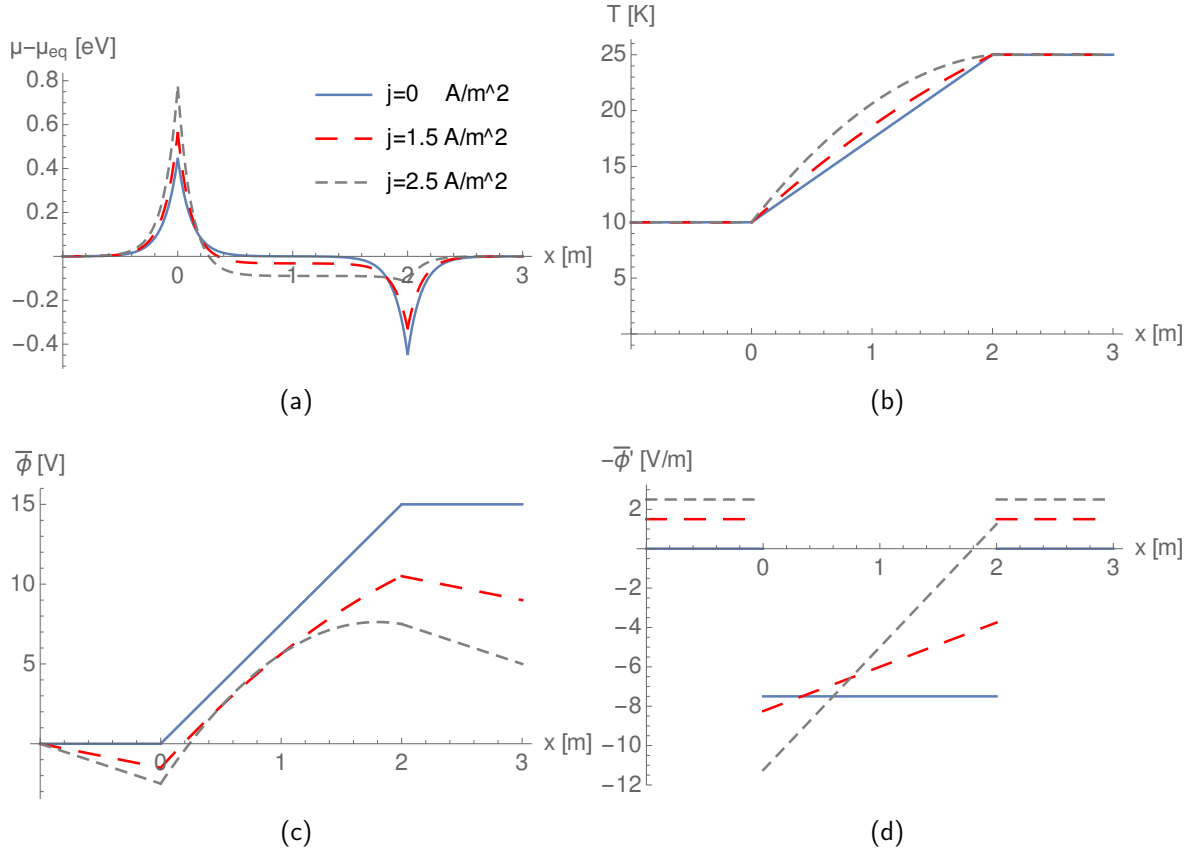


Figure 3.3.: The analytically calculated chemical potential (a), temperature (b), electrochemical potential (c) and effective field $-\bar{\phi}'$ (d) in dependence of the position for different currents. The used parameters are $T_0 = 10\text{K}$, $T_l = 25\text{K}$, $l = 2\text{m}$, $\kappa = 1\text{W/m}$, $\sigma = 1\text{S/m}$, $\xi^2 = 70$ and $\alpha = -1\text{V/m}$. The values for the parameters are not very realistic as this is merely an example, however the $\mu - \mu_{\text{eq}}$ distribution is similar for realistic values as shown later.

phonon-drag. As one can see in figure 3.3(a) the electrons accumulate at the cold side at $x = 0$ which generates a negative charge and leaves a positive charge at the hot end at $x = l$. This generates an electrical field and together with the non-equilibrium shape of μ they build an effective field $-\bar{\phi}'$ which counters the electron drift ($\alpha T'$) due to the temperature gradient in case of zero current.

When a positive current is injected into the device, the negative charge density around the surface at $x = 0$ is increased while the positive charge density at $x = l$ spreads into the bulk of the material (figure 3.3(a)). The fact that the positive charge is smeared when a current flows can be explained with the Joule-heating. Due to the current the material is heated at the rate j^2/σ which leads to a non-linear temperature slope. This in turn affects the Seebeck induced current $\alpha T'$ which is no longer a constant but position dependent. As a consequence, to have a constant current along the device the voltage induced current has to vary, which can be obtained only if the region is charged.

In figure 3.3(c) we see that the electrochemical potential gain gradually breaks down when the current is increased. This is due to the finite conductivity which generates a voltage loss that counters the Seebeck voltage.

The example of one infinitely long rod helps building a physical intuition of the Seebeck effect and how the chemical potential responds but cannot cover the physics at junctions between different materials. Therefore we will discuss another model case which is closer to a real thermoelectric generator but still analytically solvable. We assume two legs consisting of different metals (so that we can use ρ_f as given by equation (3.31)) which are connected at their ends (figure 3.4). The junctions are held at constant temperatures T_0/T_l and both legs are assumed to be of equal length l .

When we apply equation (3.24a) we find that the temperature distribution within both legs is the same as for the single rod discussed above. This gives for the total temperature distribution

$$T(x) = \begin{cases} -\frac{j^2}{2\sigma_1\kappa_1}(x^2 - lx) + \frac{T_l - T_0}{l}x + T_0 & 0 \leq x < l \\ -\frac{j^2}{2\sigma_2\kappa_2}((2l - x)^2 - l(2l - x)) + \frac{T_l - T_0}{l}(2l - x) + T_0 & l \leq x < 2l \end{cases} \quad (3.41)$$

where we have used the coordinate system introduced in figure 3.4. For the chemical potential we find the general solution

$$\frac{1}{e}\mu = \begin{cases} a_1 e^{\xi_1 x} + b_1 e^{-\xi_1 x} - \frac{c_1}{\xi_1^2} + \frac{1}{e}\mu_{\text{eq1}} & 0 \leq x < l \\ a_2 e^{\xi_2(2l-x)} + b_2 e^{-\xi_2(2l-x)} - \frac{c_2}{\xi_2^2} + \frac{1}{e}\mu_{\text{eq2}} & l \leq x < 2l \end{cases} \quad (3.42)$$

which contains four integration constants and the constants c_1 and c_2 that are defined as

$$c_1 \equiv -\frac{\alpha_1 j^2}{\sigma_1 \kappa_1}, \quad c_2 \equiv -\frac{\alpha_2 j^2}{\sigma_2 \kappa_2}. \quad (3.43)$$

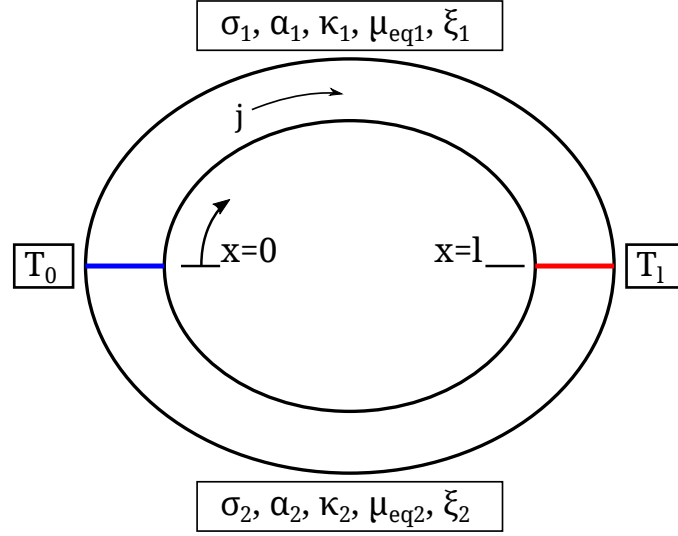


Figure 3.4.: This simple model of a thermoelectric generator consists of two legs of different materials which are described by their transport properties, their equilibrium chemical potential and the parameter $\xi \propto \sqrt{N(\mu_{eq})}$. The two legs are assumed to have the same length l .

We can determine the integration constants by applying the boundary conditions which read

$$\mu(0) = \mu(2l) , \quad (3.44a)$$

$$\mu(l^-) = \mu(l^+) , \quad (3.44b)$$

$$\mu'(0) - \mu'(2l) = j \left(\frac{1}{\sigma_1} - \frac{1}{\sigma_2} \right) + \frac{j^2 l}{2} \left(\frac{\alpha_1}{\sigma_1 \kappa_1} + \frac{\alpha_2}{\sigma_2 \kappa_2} \right) + \frac{T_l - T_0}{l} (\alpha_1 + \alpha_2) , \quad (3.44c)$$

$$\mu'(l^+) - \mu'(l^-) = j \left(\frac{1}{\sigma_2} - \frac{1}{\sigma_1} \right) + \frac{j^2 l}{2} \left(\frac{\alpha_1}{\sigma_1 \kappa_1} + \frac{\alpha_2}{\sigma_2 \kappa_2} \right) - \frac{T_l - T_0}{l} (\alpha_1 + \alpha_2) . \quad (3.44d)$$

We do not give the analytical solution of this set of equations as it is rather long and confusing and it is easy to obtain by using software that is capable of solving analytical equations like Mathematica.

So far we have treated the electrical current as an independent input parameter which is not correct for the setup given in figure 3.4. As the electrical circuit is closed at $x = 2l$ and the electrochemical potential has to be continuous we have the additional boundary condition

$$0 = \bar{\phi}(2l) - \bar{\phi}(0) = \int_0^{2l} dx \bar{\phi}'(x) . \quad (3.45)$$

With equation (3.8b) we can calculate this expression which gives

$$0 = -jl \left(\frac{1}{\sigma_1} + \frac{1}{\sigma_2} \right) + (T_l - T_0)(\alpha_2 - \alpha_1) \quad (3.46)$$

and therefore the electrical current has to fulfill

$$j = \frac{(T_l - T_0)(\alpha_2 - \alpha_1)}{l \left(\frac{1}{\sigma_1} + \frac{1}{\sigma_2} \right)} . \quad (3.47)$$

This relation is basically the total electrochemical potential difference generated by the Seebeck effect divided by the total resistance which is known as Ohm's law.

The figures 3.5(a)-3.5(e) show several quantities for the case of two materials that have the same Seebeck coefficients but different equilibrium chemical potentials. According to equation (3.47) the electrical current is zero which represents the well known fact that only the difference of the Seebeck coefficients determines the output voltage of thermoelements.

As the equilibrium values of the chemical potentials are different their electrochemical potentials are different as well if the materials are uncharged. When they are attached at the junctions the electrons diffuse from the material with the higher potential into the one with the lower potential until the electrochemical potential becomes the same. In case of non-zero but equal Seebeck coefficients there are additional charge densities generated which counter the current that would flow due to the Seebeck effect. These charges add to those already existing which is the reason for the asymmetric shape of the chemical potentials in figure 3.5(a).

The figures 3.6(a)-3.6(e) show the same quantities for two materials with Seebeck coefficients that have opposite sign. As we have imposed a temperature gradient there is a current flowing according to equation (3.47) which leads to a non-linear temperature slope. This in turn generates a charge accumulation within the bulk which is the same effect as observed for the infinitely long rod we have already discussed.

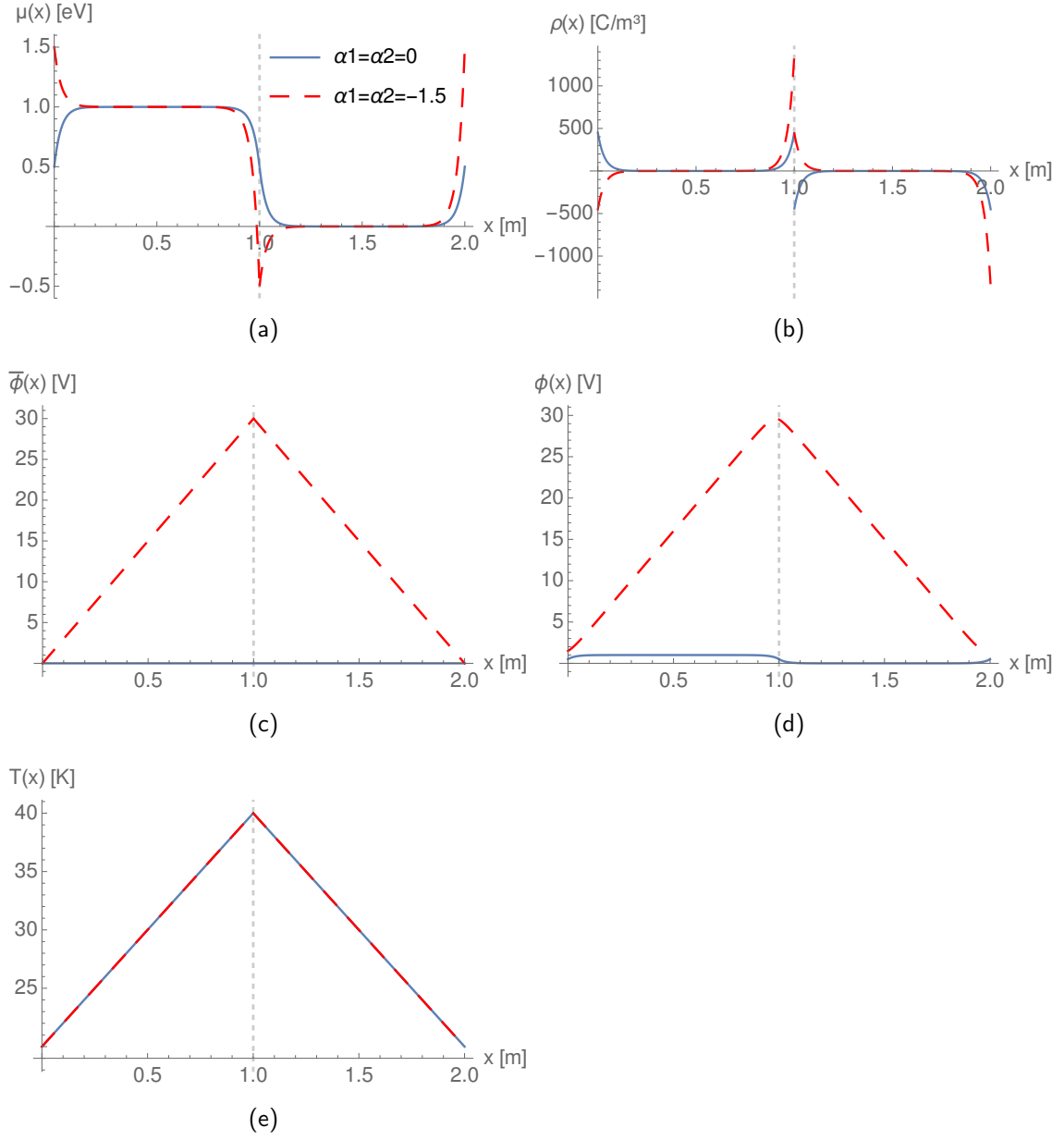


Figure 3.5.: The chemical potential (a), charge density (b), electrochemical potential (c), electrical potential (d) and the temperature (e) in dependence of the position for the case $\alpha_1 = \alpha_2$ and different equilibrium chemical potentials $\mu_{\text{eq}1} = 1\text{eV}$, $\mu_{\text{eq}2} = 0\text{eV}$. For this case there is no electrical current flowing, i.e. $j = 0$. We see that the chemical potentials are forced off their equilibrium values at the junctions which generates charge densities. In case of non-vanishing α there is an additional charging due to the Seebeck effect. The parameters used are $T_0 = 20\text{K}$, $T_l = 40\text{K}$, $\kappa_1 = \kappa_2 = 50\text{WK}^{-1}\text{m}^{-2}$, $\xi_1 = \xi_2 = 30$, $\sigma_1 = \sigma_2 = 1\text{Sm}^{-1}$

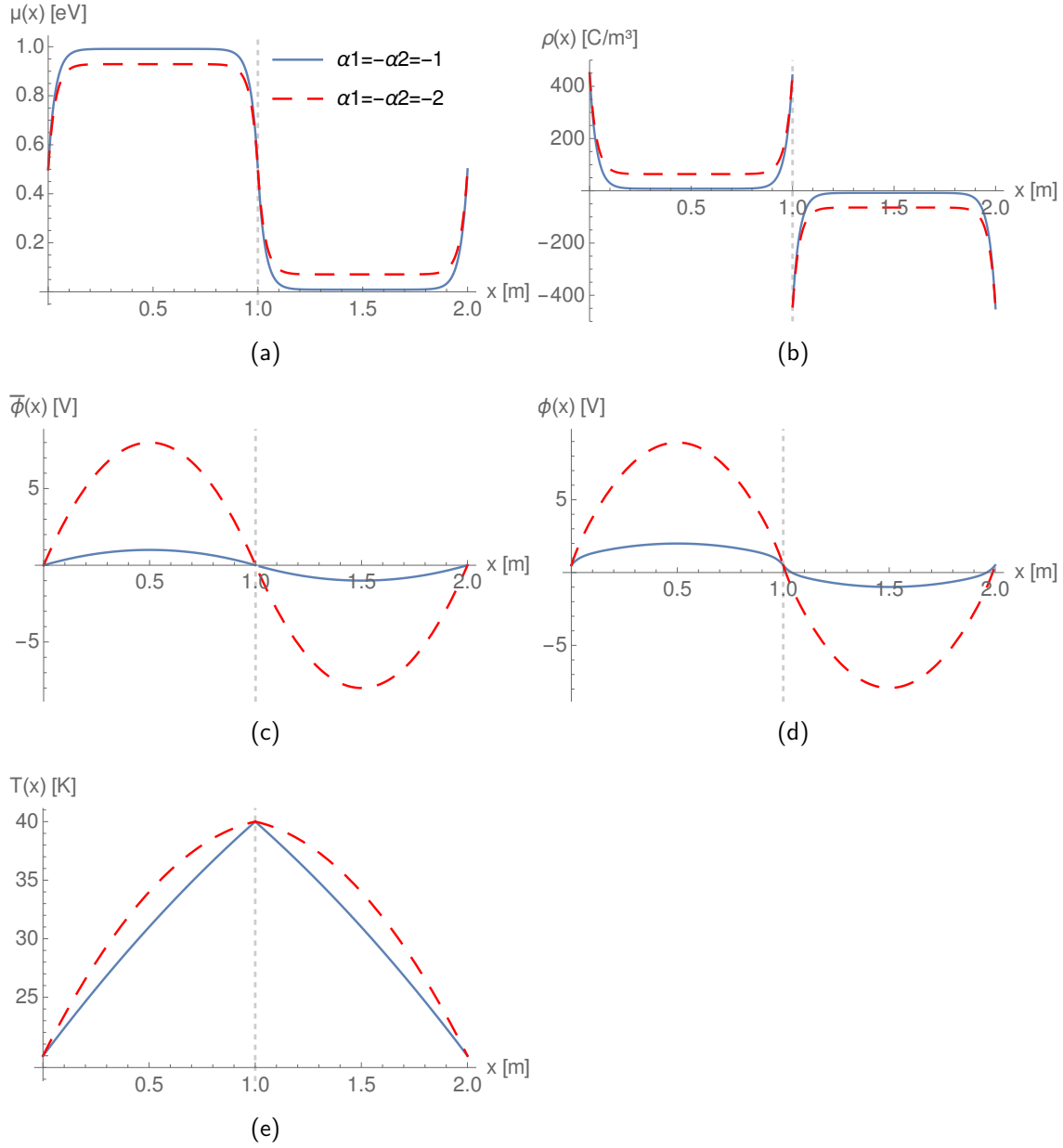


Figure 3.6.: Same as figure 3.5 but for the case $\alpha_1 = -\alpha_2$. The electrical current which flows is $j = 20 \text{ A m}^{-2}$ for $\alpha_1 = -\alpha_2 = -1 \text{ V K}^{-1}$ and $j = 40 \text{ A m}^{-2}$ for $\alpha_1 = -\alpha_2 = -2 \text{ V K}^{-1}$. As in the example with the infinitely long rod we observe a charge accumulation within the bulk for non-vanishing current due to the non-linear temperature distribution. The parameters used are the same as in figure 3.5.

4. Simulation of the full thermoelement

4.1. Model and equations

In the previous sections we have introduced the equations which describe the physics within a thermoelectric device and we have applied these equations to two analytically solvable cases. There we were restricted to metals as we needed an analytical model for the charge density ρ_f and we only used constant transport coefficients. However, most of the materials that show good thermoelectric properties are semiconductors which have a bandgap from some meV to eV . The equilibrium chemical potential typically lies inside the gap or at the edge of the band in case of highly doped semiconductors which leads to transport coefficients with a strong dependence on μ and T . This is the reason why we would like to have a simulation that calculates the chemical potential and temperature distributions for arbitrary transport coefficients and then calculates the correct efficiency subsequently.

As a first step towards a numerical simulation we have to define the geometry of the thermoelectric device (figure 4.1). We choose a two-leg device where the legs may consist of any material with μ - and T - dependent coefficients. The electrical connections are assumed to be metals held at different temperatures T_0 and T_l which are described by constant transport coefficients and the charge density model introduced in section 3.4. As we assume that the metallic regions have constant temperatures their Seebeck coefficients and their thermal conductivities are not relevant. As for the analytical two-leg device in section 3.4 we neglect surface effects and assume constant cross-sectional areas which again gives an effective one-dimensional problem with a constant electrical current density j . We have labeled the four different regions with indexes ranging from 1-4 where the regions 2 and 4 are the thermoelectric materials and 1 and 3 are the metals. The length of the metals is l_{ex} while the length of the regions 2 and 4 is l .

In the following discussion we will use different coordinate systems. The global system has its origin in the middle of region 1 according to figure 4.1. We will also make use of two local coordinate systems that have their origins at the left borders of the regions 2 and 4. With these local coordinate systems we define the global

In order to calculate the chemical potential and temperature distribution for the whole device we have to solve the equations (3.24a) and (3.24b) for every region and combine them according to the boundary conditions (3.26a) - (3.26d). When the transport coefficients depend on μ and T we can only achieve this numerically which means that we would have to discretize the whole device and solve it at once. This can be computationally demanding and numerically unstable. For this reason we apply further simplifications. We will show in the following that it is possible to mathematically decouple the equations for the four different regions and solve them independently while the main effects that stem from the junctions are preserved.

As can be seen in figure 4.1 there is a cut in region 1 where two wires are attached that connect the thermoelectric device to the load (or battery in case of a cooler). Since the wires would influence the local chemical potential in region 1 we would have to include them into the calculation as another region for a proper treatment of the whole device. We start analyzing the case of a closed device (i.e. no cut in region 1), and later we will show how to adapt the treatment to the general case. The continuity of the electrochemical potential requires

$$\bar{\phi}(0) = \bar{\phi}(2l + 2l_{\text{ex}}). \quad (4.3)$$

In analogy to the analytical solution of the two-leg device in section 3.4 this boundary condition would give the electrical current that flows through the device.

As we have assumed metals for the regions 1 and 3 we can describe them with constant transport coefficients and linearized dependence of the charge density on the chemical potential and therefore solve them analytically as shown above. In these regions the Domenicali equation (3.24a) is not necessary since the temperatures are constant and given as an input. For the charge density we use the relation

$$\rho_{fi}(\mu) = -\frac{\epsilon_0 \xi_i^2}{e}(\mu - \mu_{\text{eq } i}) \quad i \in \{2, 4\} \quad (4.4)$$

where the factors ξ_i depend on the density-of-states according to equation (3.30) and are input parameters for each metal. The chemical potentials within the metallic regions are solutions of equation (3.24b) and read

$$\frac{1}{e}\mu_1(x) = a_1 e^{\xi_1(x - \frac{l_{\text{ex}}}{2})} + b_1 e^{-\xi_1(x + \frac{l_{\text{ex}}}{2})} + \frac{1}{e}\mu_{\text{eq } 1}, \quad (4.5)$$

$$\frac{1}{e}\mu_3(x) = a_3 e^{\xi_3(x - (l + \frac{3l_{\text{ex}}}{2}))} + b_3 e^{-\xi_3(x - (l + \frac{l_{\text{ex}}}{2}))} + \frac{1}{e}\mu_{\text{eq } 3}. \quad (4.6)$$

We have chosen the offsets in the exponentials so that they become zero at the junctions according to equation (4.1) which ensures easier to handle expressions. The a_i and b_i are integration constants which determine the shape of the final solutions.

The boundary conditions (3.26a) and (3.26b) applied to all junctions give

$$\left\{ \begin{array}{l} \mu_1\left(\frac{l_{\text{ex}}}{2}\right) = \mu_2(0) \\ \frac{\epsilon_2}{e}\mu'_2(0) - \frac{1}{e}\mu'_1\left(\frac{l_{\text{ex}}}{2}\right) = j\left(\frac{\epsilon_2}{\sigma_2(0)} - \frac{1}{\sigma_1}\right) + \epsilon_2\alpha_2(0)T'_2(0) \end{array} \right\} \text{ for } x = \frac{l_{\text{ex}}}{2} \quad (4.7)$$

$$\left\{ \begin{array}{l} \mu_2(l) = \mu_3\left(l + \frac{l_{\text{ex}}}{2}\right) \\ \frac{1}{e}\mu'_3\left(l + \frac{l_{\text{ex}}}{2}\right) - \frac{\epsilon_2}{e}\mu'_2(l) = j\left(\frac{1}{\sigma_3} - \frac{\epsilon_2}{\sigma_2(l)}\right) - \epsilon_2\alpha_2(l)T'_2(l) \end{array} \right\} \text{ for } x = l + \frac{l_{\text{ex}}}{2} \quad (4.8)$$

$$\left\{ \begin{array}{l} \mu_3\left(l + \frac{3l_{\text{ex}}}{2}\right) = \mu_4(l) \\ -\frac{\epsilon_4}{e}\mu'_4(l) - \frac{1}{e}\mu'_3\left(l + \frac{3l_{\text{ex}}}{2}\right) = j\left(\frac{\epsilon_4}{\sigma_4(l)} - \frac{1}{\sigma_3}\right) - \epsilon_4\alpha_4(l)T'_4(l) \end{array} \right\} \text{ for } x = l + \frac{3l_{\text{ex}}}{2} \quad (4.9)$$

$$\left\{ \begin{array}{l} \mu_4(0) = \mu_1\left(-\frac{l_{\text{ex}}}{2}\right) \\ \frac{1}{e}\mu'_1\left(-\frac{l_{\text{ex}}}{2}\right) + \frac{\epsilon_4}{e}\mu'_4(0) = j\left(\frac{1}{\sigma_1} - \frac{\epsilon_4}{\sigma_4(0)}\right) + \epsilon_4\alpha_4(0)T'_2(0) \end{array} \right\} \text{ for } x = 2l + \frac{3l_{\text{ex}}}{2} \quad (4.10)$$

and with the analytical solutions of regions 1 and 3 (equations (4.5) and (4.6)) they become

$$\left\{ \begin{array}{l} a_1 + b_1e^{-\xi_1 l_{\text{ex}}} + \frac{1}{e}\mu_{\text{eq1}} = \frac{1}{e}\mu_2(0) \\ \frac{\epsilon_2}{e\xi_1}\mu'_2(0) - a_1 + b_1e^{-\xi_1 l_{\text{ex}}} = \underbrace{\frac{1}{\xi_1}\left[j\left(\frac{\epsilon_2}{\sigma_2(0)} - \frac{1}{\sigma_1}\right) + \epsilon_2\alpha_2(0)T'_2(0)\right]}_{\lambda} \end{array} \right\} \text{ for } x = \frac{l_{\text{ex}}}{2} \quad (4.11)$$

$$\left\{ \begin{array}{l} \frac{1}{e}\mu_2(l) = a_3e^{-\xi_3 l_{\text{ex}}} + b_3 + \frac{1}{e}\mu_{\text{eq3}} \\ a_3e^{-\xi_3 l_{\text{ex}}} - b_3 - \frac{\epsilon_2}{e\xi_3}\mu'_2(l) = \underbrace{\frac{1}{\xi_3}\left[j\left(\frac{1}{\sigma_3} - \frac{\epsilon_2}{\sigma_2(l)}\right) - \epsilon_2\alpha_2(l)T'_2(l)\right]}_{\delta} \end{array} \right\} \text{ for } x = l + \frac{l_{\text{ex}}}{2} \quad (4.12)$$

$$\left\{ \begin{array}{l} a_3 + b_3e^{-\xi_3 l_{\text{ex}}} + \frac{1}{e}\mu_{\text{eq3}} = \mu_4(l) \\ \frac{\epsilon_4}{e}\mu'_4(l) + a_3 - b_3e^{-\xi_3 l_{\text{ex}}} = -\underbrace{\frac{1}{\xi_3}\left[j\left(\frac{\epsilon_4}{\sigma_4(l)} - \frac{1}{\sigma_3}\right) - \epsilon_4\alpha_4(l)T'_4(l)\right]}_{\gamma} \end{array} \right\} \text{ for } x = l + \frac{3l_{\text{ex}}}{2} \quad (4.13)$$

$$\left\{ \begin{array}{l} \mu_4(0) = a_1e^{-\xi_1 l_{\text{ex}}} + b_1 + \frac{1}{e}\mu_{\text{eq1}} \\ a_1e^{-\xi_1 l_{\text{ex}}} - b_1 + \frac{\epsilon_4}{e\xi_1}\mu'_4(0) = \underbrace{\frac{1}{\xi_1}\left[j\left(\frac{1}{\sigma_1} - \frac{\epsilon_4}{\sigma_4(0)}\right) + \epsilon_4\alpha_4(0)T'_2(0)\right]}_{\beta} \end{array} \right\} \text{ for } x = 2l + \frac{3l_{\text{ex}}}{2} . \quad (4.14)$$

where we have defined the quantities λ , δ , γ and β . The eight boundary conditions depend on the integration constants and on the values of the chemical potentials

and their derivatives at the junctions in a linear fashion. Therefore it is possible to eliminate the four integration constants a_i and b_i analytically which leaves expressions that couple only the active regions, i.e. regions 2 and 4,

$$\frac{1}{e} \left[\mu_2(0) - \mu_{\text{eq1}} - \frac{\epsilon_2}{\xi_1} \mu'_2(0) \right] + \lambda = e^{-\xi_1 l_{\text{ex}}} \left(\frac{1}{e} \left[\mu_4(0) - \mu_{\text{eq1}} + \frac{\epsilon_4}{\xi_1} \mu'_4(0) \right] - \beta \right), \quad (4.15a)$$

$$\frac{1}{e} \left[\mu_2(l) - \mu_{\text{eq3}} + \frac{\epsilon_2}{\xi_1} \mu'_2(l) \right] + \delta = e^{-\xi_3 l_{\text{ex}}} \left(\frac{1}{e} \left[\mu_4(l) - \mu_{\text{eq3}} - \frac{\epsilon_4}{\xi_3} \mu'_4(l) \right] - \gamma \right), \quad (4.15b)$$

$$\frac{1}{e} \left[\mu_4(0) - \mu_{\text{eq1}} - \frac{\epsilon_4}{\xi_1} \mu'_4(0) \right] + \beta = e^{-\xi_1 l_{\text{ex}}} \left(\frac{1}{e} \left[\mu_2(0) - \mu_{\text{eq1}} + \frac{\epsilon_2}{\xi_1} \mu'_2(0) \right] - \lambda \right), \quad (4.15c)$$

$$\frac{1}{e} \left[\mu_4(l) - \mu_{\text{eq3}} + \frac{\epsilon_4}{\xi_3} \mu'_4(l) \right] + \gamma = e^{-\xi_3 l_{\text{ex}}} \left(\frac{1}{e} \left[\mu_2(l) - \mu_{\text{eq3}} - \frac{\epsilon_2}{\xi_1} \mu'_2(l) \right] - \delta \right). \quad (4.15d)$$

These four relations only contain μ and μ' of regions 2 and 4, leading to a complexity reduction of the problem from four coupled regions to two. Since the terms on the left-hand side and the terms within the outer brackets on the right-hand side of the equations have the same order of magnitude we can apply a further simplification and set the right-hand side to zero. This only holds when the exponential is sufficiently small. This, however, is always the case as the following reasoning shows. Metals usually have a large density-of-states at the Fermi level, for example copper has $N(\epsilon_f) \approx 10^{47} J^{-1} m^{-3}$ (obtained from WIEN2K-DFT simulation [14–20] + BoltzTraP [21]). According to equation (3.30) this gives for the inverse decay length $\xi \approx 10^{10} m^{-1}$. The length of the metallic connections (l_{ex}) in real devices are always much larger than $1 \mu m$ hence we will assume this value as a lower limit. With this we get for the exponential

$$e^{-\xi l_{\text{ex}}} \approx e^{-10^4} \approx 10^{-4343} \quad (4.16)$$

which ensures that we are always allowed to set the exponentials to zero. The

boundary conditions then become

$$\frac{1}{e} \left[\mu_2(0) - \mu_{\text{eq1}} - \frac{\epsilon_2}{\xi_1} \mu'_2(0) \right] = -\frac{1}{\xi_1} \left[j \left(\frac{\epsilon_2}{\sigma_2(0)} - \frac{1}{\sigma_1} \right) + \epsilon_2 \alpha_2(0) T'_2(0) \right] , \quad (4.17a)$$

$$\frac{1}{e} \left[\mu_2(l) - \mu_{\text{eq3}} + \frac{\epsilon_2}{\xi_1} \mu'_2(l) \right] = -\frac{1}{\xi_3} \left[j \left(\frac{1}{\sigma_3} - \frac{\epsilon_2}{\sigma_2(l)} \right) - \epsilon_2 \alpha_2(l) T'_2(l) \right] , \quad (4.17b)$$

$$\frac{1}{e} \left[\mu_4(0) - \mu_{\text{eq1}} - \frac{\epsilon_4}{\xi_1} \mu'_4(0) \right] = -\frac{1}{\xi_1} \left[j \left(\frac{1}{\sigma_1} - \frac{\epsilon_4}{\sigma_4(0)} \right) + \epsilon_4 \alpha_4(0) T'_2(0) \right] , \quad (4.17c)$$

$$\frac{1}{e} \left[\mu_4(l) - \mu_{\text{eq3}} + \frac{\epsilon_4}{\xi_3} \mu'_4(l) \right] = -\frac{1}{\xi_3} \left[j \left(\frac{\epsilon_4}{\sigma_4(l)} - \frac{1}{\sigma_3} \right) - \epsilon_4 \alpha_4(l) T'_4(l) \right] \quad (4.17d)$$

which are four robin-type boundary conditions. It can be noticed that the first two equations (4.17a), (4.17b) only depend on μ_2 while the other two (4.17c), (4.17d) only depend on μ_4 . This means that we are now left with two completely independent regions we can solve separately in contrast to the initial four coupled regions.

The temperature distributions in the regions 2 and 4 are determined by the Domenicali equation (3.24a) and the corresponding boundary condition (3.26c) which reads for this specific case

$$T_2(0) = T_4(0) = T_0 , \quad (4.18a)$$

$$T_2(l) = T_4(l) = T_l . \quad (4.18b)$$

Overall we have the differential equations

$$\frac{j^2}{\sigma_2} + \kappa'_2 T'_2 + \kappa_2 T''_2 - T_2 j \alpha'_2 = 0 , \quad (4.19a)$$

$$-\frac{1}{e} \mu''_2 = \frac{\rho f_2}{\epsilon_0 \epsilon_2} + \frac{j}{\sigma_2^2} \sigma'_2 - \alpha'_2 T'_2 - \alpha_2 T''_2 \quad (4.19b)$$

for the region 2 and

$$\frac{j^2}{\sigma_4} + \kappa'_4 T'_4 + \kappa_4 T''_4 - T_4 (-j) \alpha'_4 = 0 , \quad (4.20a)$$

$$-\frac{1}{e} \mu''_4 = \frac{\rho f_4}{\epsilon_0 \epsilon_4} + \frac{(-j)}{\sigma_4^2} \sigma'_4 - \alpha'_4 T'_4 - \alpha_4 T''_4 \quad (4.20b)$$

for the region 4 where the minus sign of the current takes into account the reverse direction of the coordinate system introduced by equation (4.1). Together with the boundary conditions (4.18a), (4.18b) and (4.17a)-(4.17d) we have a full set of equations which we are going to solve numerically. Once we have the solutions for

the regions 2 and 4 we can obtain the a_i and b_i which determine the solutions in the regions 1 and 3 by solving the equations (4.11)-(4.14) with the simplification $e^{-\xi_i l_{\text{ex}}} \rightarrow 0$. This eventually gives for the integration constants

$$a_1 = \frac{1}{2} \left[\frac{1}{e} \mu_2(0) - \frac{1}{e} \mu_{\text{eq}1} + \frac{1}{\xi_1} \left(\frac{\epsilon_2}{e} \mu_2'(0) - j \left(\frac{\epsilon_2}{\sigma_2(0)} - \frac{1}{\sigma_1} \right) - \epsilon_2 \alpha_2(0) T_2'(0) \right) \right] \quad (4.21a)$$

$$b_1 = \frac{1}{2} \left[\frac{1}{e} \mu_4(0) - \frac{1}{e} \mu_{\text{eq}1} + \frac{1}{\xi_1} \left(\frac{\epsilon_4}{e} \mu_4'(0) + j \left(\frac{\epsilon_4}{\sigma_4(0)} - \frac{1}{\sigma_1} \right) - \epsilon_4 \alpha_4(0) T_4'(0) \right) \right] \quad (4.21b)$$

$$a_3 = \frac{1}{2} \left[\frac{1}{e} \mu_4(l) - \frac{1}{e} \mu_{\text{eq}3} - \frac{1}{\xi_3} \left(\frac{\epsilon_4}{e} \mu_4'(l) - j \left(\frac{1}{\sigma_3} - \frac{\epsilon_4}{\sigma_4(l)} \right) - \epsilon_4 \alpha_4(l) T_4'(l) \right) \right] \quad (4.21c)$$

$$b_3 = \frac{1}{2} \left[\frac{1}{e} \mu_2(l) - \frac{1}{e} \mu_{\text{eq}3} - \frac{1}{\xi_3} \left(\frac{\epsilon_2}{e} \mu_2'(l) + j \left(\frac{1}{\sigma_3} - \frac{\epsilon_2}{\sigma_2(l)} \right) - \epsilon_2 \alpha_2(l) T_2'(l) \right) \right] . \quad (4.21d)$$

For now we have treated the model (figure 4.1) as if the cut in region 1 would not be there. With the same argument we have used to split the regions 2 and 4 we can argue that if there was a cut with attached wires the distortion of the chemical potential would not influence the junctions of region 1 with the regions 2 and 4. Since the transport coefficients are assumed to be constants in metals the local distortion of the chemical potential would not affect the transport properties of the whole device either. Therefore the initial assumption of a non-existent cut is retrospectively justified. However, we have to set up the boundary condition of the continuous electrochemical potential for the whole system which is the thermoelectric device plus the attached load. When we apply the equation (2.16) we get

$$0 = \oint dx \bar{\phi}'(x) = \int_0^{2l+2l_{\text{ex}}} dx \bar{\phi}'(x) - U = - \int_0^{2l+2l_{\text{ex}}} dx \left(\frac{j}{\sigma(x)} + \alpha(x) T'(x) \right) - U \quad (4.22)$$

where U is the voltage at the load or the attached battery respectively. The load resistance is connected to the current and the voltage by Ohm's law which reads

$$R_{\text{load}} = \frac{U}{jA} \quad (4.23)$$

with the cross-sectional area A . For a given load the equations (4.22) and (4.23) define the electrical current that flows through the device. Since it is difficult to include the condition of one specific load resistance in the calculation we treat j as an input parameter. The output voltage is then calculated after we have obtained

the solution for the chemical potential and the temperature. Eventually one can calculate the corresponding load resistance with equation (4.23) and then vary the electrical current until the load resistance matches the sought value.

4.2. Numerical implementation

In chapter 4.1 we have derived the equations and boundary conditions for the thermoelectric device and we have seen that the equations of the different regions can be decoupled under some circumstances. However, the remaining equations for temperature and chemical potential are mutually coupled within each region and the transport coefficients depend on the sought quantities as well. Therefore we need an algorithm to obtain the solutions numerically. For the implementation we use *Mathematica* 10 which provides several built-in routines. Furthermore it is possible to create graphical user interfaces which was an aim in order to simplify the usability of the final program.

For the solution we choose an iterative self-consistent strategy. We make an initial guess for the temperature and the chemical potential that we call $T_i^{[0]}(x)$ and $\mu_i^{[0]}(x)$ where the superscript is the iteration count (figure 4.2). For the starting distribution we choose

$$T_i^{[0]}(x) = \frac{T_l - T_0}{l}x + T_0, \quad (4.24)$$

$$\mu_i^{[0]}(x) = \mu_{\text{eq-i}}(T_i^{[0]}(x)) \quad (4.25)$$

where $\mu_{\text{eq-i}}(T)$ denotes the equilibrium chemical potential, i.e. the chemical potential for which the charge density at the given temperature T is zero.

With these starting distributions we can calculate the position dependent transport coefficients which read

$$\sigma_i^{[0]}(x) \equiv \sigma_i(\mu_i^{[0]}(x), T_i^{[0]}(x)), \quad (4.26a)$$

$$\alpha_i^{[0]}(x) \equiv \alpha_i(\mu_i^{[0]}(x), T_i^{[0]}(x)), \quad (4.26b)$$

$$\kappa_i^{[0]}(x) \equiv \kappa_i(\mu_i^{[0]}(x), T_i^{[0]}(x)), \quad (4.26c)$$

where the index i stands for the region and can have the values 2 or 4. By inserting these functions into the equations (4.19) we get

$$\frac{j^2}{\sigma_2^{[0]}(x)} + \kappa_2^{[0]}(x)'T_2(x)' + \kappa_2^{[0]}(x)T_2(x)'' - T_2(x)j\alpha_2^{[0]}(x)' = 0, \quad (4.27a)$$

$$-\frac{1}{e}\mu_2(x)'' = \frac{\rho f_2}{\epsilon_0 \epsilon_2} + \frac{j}{\sigma_2^{[0]}(x)^2}\sigma_2^{[0]}(x)' - \alpha_2^{[0]}(x)'T_2(x)' - \alpha_2^{[0]}(x)T_2(x)'' \quad (4.27b)$$

for the region 2 and a similar expression is obtained for region 4. The equation (4.27a) is now a linear differential equation which does not depend on $\mu(x)$ explicitly and therefore can be solved for $T(x)$ with a standard solver. For the implementation we use the standard *Mathematica* routine *NDSolve* which internally uses a Runge-Kutta solver plus a shooting method for problems with Dirichlet boundary conditions as we have here.

The equation (4.27b) for $\mu_2(x)$ still contains the charge density $\rho_f(\mu_2(x), T(x))$ which depends on $\mu_2(x)$. In principle we could proceed as we did with the transport coefficients and just insert the previous solution but the problem is that the charge density usually has a very strong dependence on the chemical potential. That simple strategy would increase the likelihood of overshooting and dramatically affect the stability of the numerical solver. This may lead to slow or even no convergence in the iteration cycle. Therefore we linearize the charge density with respect to the previous solution of the chemical potential $\mu_2^{[0]}(x)$ which reads

$$\rho_{f2}(x) \approx \underbrace{\rho_{f2}(\mu_2^{[0]}(x), T^{[0]}(x))}_{\rho_{f2}^{[0]}(x)} + \underbrace{\frac{\partial \rho_{f2}}{\partial \mu}(\mu_2^{[0]}(x), T^{[0]}(x))}_{\frac{\partial \rho_{f2}^{[0]}}{\partial \mu}(x)} (\mu_2(x) - \mu_2^{[0]}(x)) . \quad (4.28)$$

With this simplification the equation (4.27b) becomes

$$-\frac{1}{e}\mu_2(x)'' = \frac{1}{\epsilon_0\epsilon_2} \left[\rho_{f2}^{[0]}(x) + \frac{\partial \rho_{f2}^{[0]}}{\partial \mu}(x) (\mu_2(x) - \mu_2^{[0]}(x)) \right] + \quad (4.29)$$

$$+ \frac{j}{\sigma_2^{[0]}(x)^2} \sigma_2^{[0]}(x)' - \alpha_2^{[0]}(x)' T_2(x)' - \alpha_2^{[0]}(x) T_2(x)'' \quad (4.30)$$

where the $T_2(x)$ is the solution of equation (4.27a) we have already calculated. With the given simplifications the equation (4.30) is linear in the chemical potential and we can apply an appropriate algorithm to obtain a solution. As we have robin-type boundary conditions which contain the first derivatives as well as the value of the chemical potential itself at the junctions, the shooting method proves very inefficient as we would have to vary $\mu_2(0)$ and $\mu_2(0)'$ until $\mu_2(l)$ and $\mu_2(l)'$ show the correct values. Furthermore the shooting method results are unstable as the solution is rather sensitive on the starting values of μ_2 . Therefore we choose the finite-element method as it has proven to be stable and to have good performance. The *NDSolve* framework already provides a finite-element solver in *Mathematica* 10 which we use for the implementation. We know from the analytical solutions in chapter 3.4 that the chemical potential has its steepest change at the junctions as it tries to match the equilibrium value of the attached metal. To take this into

account we use elements with two different element sizes Δx ,

$$\Delta x = \begin{cases} \frac{n_{\text{dep}}}{l_{\text{dep}}} & 0 \leq x < l_{\text{dep}} \\ \frac{n_l}{l} & l_{\text{dep}} \leq x < l - l_{\text{dep}} \\ \frac{n_{\text{dep}}}{l_{\text{dep}}} & l - l_{\text{dep}} \leq x < l \end{cases} \quad (4.31)$$

where the values n_l , n_{dep} and the size of the areas around the junctions l_{dep} may be chosen freely.

After obtaining the numerical solutions $T_2(x)$ and $\mu_2(x)$ for the temperature and the chemical potential we mix them with the solutions of the previous step according to the relations

$$T_2^{[1]}(x) \equiv T_2^{[0]}(x) + \delta \left(T_2(x) - T_2^{[0]}(x) \right) , \quad (4.32)$$

$$\mu_2^{[1]}(x) \equiv \mu_2^{[0]}(x) + \delta \left(\mu_2(x) - \mu_2^{[0]}(x) \right) , \quad (4.33)$$

where δ is the so-called mixing parameter (not to be confused with the δ defined in equation (4.12)). For the value $\delta = 1$ the new solutions would coincide with the calculated ones while a value of $\delta = 0$ would mean that we stick to the initially chosen distributions which, of course, would not make sense. The reason for this mixing is that it can happen that the numerical solutions oscillate around the real solution which can be prevented by a reduction of the mixing-parameter. With these new distributions for the temperature and the chemical potential the whole procedure can be repeated until the solution does not change any more, i.e. it is converged (figure 4.2). The convergence is checked with the quantities

$$\Delta T_2 \equiv \text{Max} \left\{ T_2^{[i]}(x) - T_2^{[i-1]}(x) \right\} \quad (4.34a)$$

$$\Delta \mu_2 \equiv \text{Max} \left\{ \mu_2^{[i]}(x) - \mu_2^{[i-1]}(x) \right\} . \quad (4.34b)$$

Both values are compared to specified termination values and if both are smaller the iteration cycle stops, i.e. when

$$(\Delta T_2 < T_{\text{res}}) \ \& \ (\Delta \mu_2 < \mu_{\text{res}}) \quad (4.35)$$

is true.

With the chemical potential and the temperature distributions of region 2 and 4 we can calculate the integration constants a_i and b_i with the equations (4.21a)-(4.21d) providing the solutions of the regions 1 and 3. Now we can combine the different solutions according to the equations (4.1) and (4.2) which gives the complete $\mu(x)$ and $T(x)$.

With these quantities we can determine the output voltage according to equation (4.22) where we calculate the integral in the regions 1 and 3 analytically and in

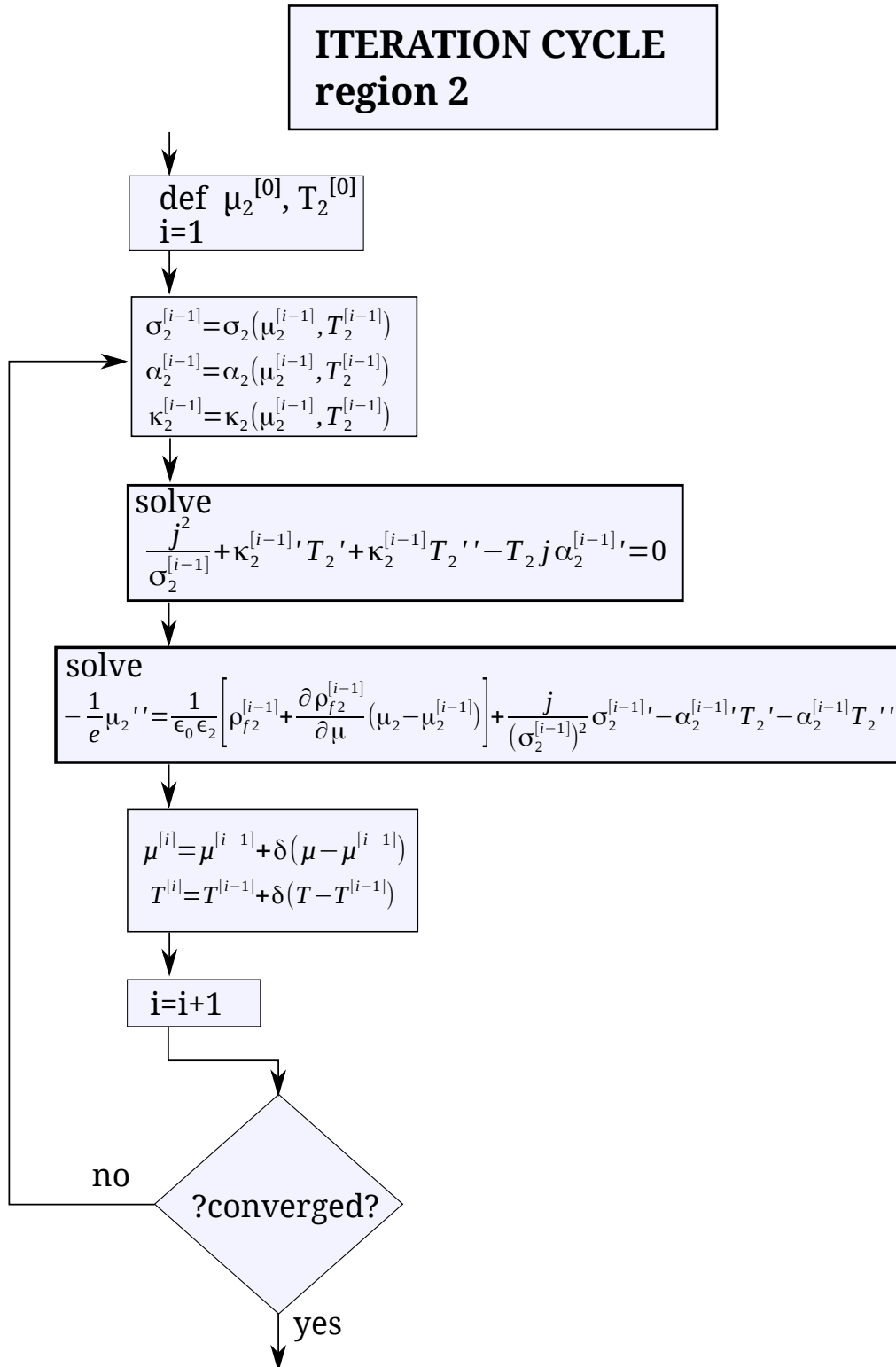


Figure 4.2.: Flow chart of the iteration cycle for the solution in the region 2. The solver for region 4 works exactly the same except from the slightly different equations (4.20a), (4.20b).

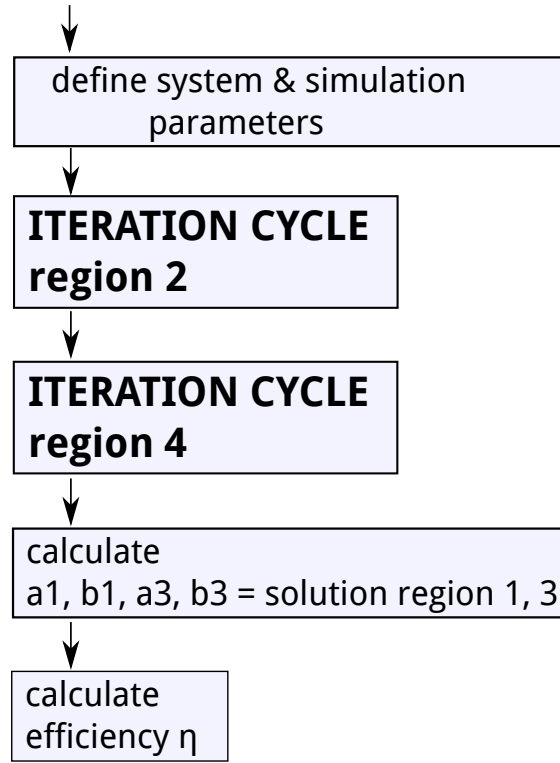


Figure 4.3.: Flow chart of the of the total program. At the beginning the input parameters, transport coefficient functions and the system geometry have to be defined. Then the program calculates the numeric solutions of the regions 2 and 4 and the integration constants i.e. the solutions of regions 1 and 3 subsequently. Finally the efficiency can be obtained by using equation (4.36) or (4.37) respectively.

the regions 2 and 4 numerically with finite-element integration using the same non-equidistant elements defined by equation (4.31).

The last step is to calculate the output efficiency or the cooling efficiency in case the device operates as a cooler. The efficiency is defined as

$$\eta_{\text{gen}} \equiv \frac{j\Delta\bar{\phi}}{\pm(j_{Q2}(T_h) + j_{Q4}(T_h))} \quad (4.36)$$

for a generator and as

$$\eta_{\text{cool}} \equiv \frac{\pm(j_{Q2}(T_c) + j_{Q4}(T_c))}{j\Delta\bar{\phi}} \quad (4.37)$$

for a cooler. The heat currents j_{Qi} are defined by equation (2.17) and their argument means that they are evaluated at the junction where the temperature is hottest (T_h) or coldest (T_c). The \pm sign in front of the heat currents accounts for the fact that

they are counted positive when they flow from the junction into the device and the sign depends whether they are evaluated at $x = 0$ or $x = l$. The total program structure is shown in figure 4.3.

4.3. Optimization of the chemical potential position

Our simulation calculates the real position of the chemical potential within a thermoelectric device which does not need to be the equilibrium value. Therefore it can happen that the chemical potential in a certain region stays at a position where the transport coefficients have inefficient values while they might have optimal values for a different chemical potential position.

The actual position of the chemical potential can be influenced by doping which lead to the idea that we could calculate a doping distribution for which the efficiency of the whole device shows a maximum. We do not discuss in this work the stability of this doping distribution in a real device or how it can be established physically. We simply treat the doping as an additional charge density that is position dependent,

$$\rho_{fi}(\mu(x), T(x)) \rightarrow \rho_{fi}(\mu_i(x), T_i(x)) + ed_i(x) \quad (4.38)$$

where e is the positive elementary charge. This convention ensures that an electron donor corresponds to $d_i(x) > 0$ whereas an electron acceptor is represented by $d_i(x) < 0$. If the dopant has one more or less valence electrons than the original atom, the function $d_i(x)$ is equivalent to the dopant concentration.

In general the efficiency is a functional of all transport coefficients and, which is relevant here, the charge density. As ρ_{fi} depends on the doping function $d_i(x)$ the idea is to maximize the efficiency with respect to the doping function. The numerical maximization of a continuous function is in principle an infinitely dimensional problem which is the reason why we only take n points $\{d_i(x_j)\}$ which we vary. The continuous doping function is then calculated by linear interpolation. With this trick we have reduced the dimension of the optimization problem to n .

For every evaluation of the efficiency η we have to run the full simulation which can be rather demanding. Therefore optimization methods where we have to calculate a gradient are not appropriate as they require many evaluations in order to determine the derivatives. A method which requires few evaluations of the quantity we want to maximize, which is called objective function, is the so-called Nelder-Mead method [22]. For this procedure we have to specify $n + 1$ initial sets of parameters which are basically $n + 1$ points in the n -dimensional optimization space. These points build a simplex which is the simplest geometric form that accounts for the dimensionality, i.e. a triangle in two dimensions or a straight line in one dimension. Then the objective function is evaluated for each of the $n + 1$ point in the parameter space and the point with the worst value is moved into the direction

where a better value is expected due to the value of the other points. When the algorithm is converged in the end it happens that all points in the parameter space approach the same value. For the termination criterion we use the function

$$\Delta \equiv \frac{1}{2} (|\eta[d_{\text{worst}}(x)]_k - \eta[d_{\text{worst}}(x)]_{k-1}| + |\eta[d_{\text{worst}}(x)]_k - \eta[d_{\text{best}}(x)]_k|) \quad (4.39)$$

where k is the iteration index and $d_{\text{worst}}(x)$ / $d_{\text{best}}(x)$ correspond to the worst / best points in the parameter space. The optimization stops when Δ is smaller than some defined value.

Additionally we have introduced upper and lower limits for the doping function as we are usually bound to physical limits when a material is doped. In the algorithm it is checked whether a new calculated point in the parameter space would lie outside the boundaries and if that is the case, the point is discarded and the best point which still lies inside the boundaries is taken. This ensures that the optimization is done within the defined maximum values of the doping function.

5. Results and interpretation

We are interested in the effect the actual chemical potential and temperature distributions $\mu(x)$ and $T(x)$ have on the efficiency of a thermoelectric device. For that reason we have done simulations of different materials which are used in thermoelectric generators or show interesting features. The program needs the transport coefficients and the charge density in dependence of the chemical potential and temperature. One way to obtain these functions is to perform a DFT simulation of the sought material using, for example, WIEN2K [14] and then to employ the band-structure as an input for BoltzTraP [21]. This program calculates the transport properties using the linearized Boltzmann equation in the relaxation time approximation. Furthermore the relaxation time is assumed to be independent of the energy which makes it a multiplicative factor. Note that BoltzTraP only calculates the electronic properties. Therefore the heat conductivity needs to be adapted if the transport by phonons is relevant. The following discussions focus on the qualitative behavior of the chemical potential and the impact it has on the efficiency. The simplification of a constant relaxation time is sufficient for this purpose.

In this work we discuss three different materials: Bi_2Te_3 , SrTiO_3 and FeSb_2 . For all the simulations we assume an electrical conductivity for the regions 1 and 3 that is approximately the value of copper at 300K, i.e. $\sigma_i = 10^8 \text{Sm}^{-1}$ $i \in \{1, 3\}$. For the decay length we use $\xi_i = 10^4 \mu\text{m}^{-1}$ $i \in \{1, 3\}$ if not stated differently. This value corresponds to $N(\epsilon_f) \approx 10^{47} \text{m}^{-3} \text{J}^{-1}$ which is the same order of magnitude as the density-of-states of copper.

Furthermore we test the thermoelectric efficiency the program calculates against the averaged figures of merit and the engineering figure of merit (see chapters 2.2 and 2.3) and discuss the origin of possible differences.

5.1. Bi_2Te_3

Bismuth telluride is one of the most industrially used thermoelectric materials. It is a narrow band-gap ($E_{\text{gap}} \approx 0.11 \text{eV}$ [23]) semiconductor which is used p- as well as n-doped. For the unit cell volume we have used $V_{uc} = 5.01 * 10^{-28} \text{m}^3$ [24] and for the relaxation time $\tau = 2.2 * 10^{-14} \text{s}$ [23]. The phononic contribution to the heat conductivity was assumed to be temperature independent and was added to the electronic heat conductivity, i.e. $\kappa_{ph} \approx 1 \text{Wm}^{-1} \text{K}^{-1}$ [25], $\kappa = \kappa_{el} + \kappa_{ph}$. We have applied the doping in the same way as explained in chapter 4.3. For the doping

concentration we have used

$$d_n = +5 * 10^{24} m^{-3} \text{ for n-doped-}, \quad (5.1)$$

$$d_p = -5 * 10^{24} m^{-3} \text{ for p-doped Bi}_2\text{Te}_3 \quad (5.2)$$

which are typical carrier concentration in doped bismuth telluride [23]. The figure 5.1 gives an example of the calculated μ -distribution. We have used n- and p-doped bismuth telluride for the two legs and the temperatures $T_0 = 300K$ and $T_l = 600K$ (see figure 4.1 for the convention). The equilibrium chemical potentials of the metals are $\mu_{eq-i} = 4.73eV$ $i \in \{1, 3\}$ which lies approximately in the middle of the band-gap. For the dielectric permittivity of bismuth telluride we have used $\epsilon = 100$ which is the same order of magnitude as suggested in Ref. [26]. For illustrative purposes we use a length of $l = l_{ex} = 2\mu m$ even if real devices have usually much longer legs. However, this length scale allows for an easier visualization of the behavior near the junctions. Real size devices display similar effects and will be discussed in the end of this section.

We see (figure 5.1) that the chemical potential bends towards the equilibrium value of the metal at the junctions. However, the Bi_2Te_3 also slightly distorts the chemical potential within the metal which is shown in the inset of figure 5.1(a). The figure 5.1(b) compares the calculated chemical potential in region 2 with the equilibrium chemical potential (i.e. zero local charge density) assuming a linear temperature slope $\mu_{eq}(T_0 + x\Delta T/l)$ and for the calculated temperature distribution $\mu_{eq}(T_2(x))$. In the bulk the equilibrium chemical potential for the calculated temperature is in very good agreement with the calculated $\mu(x)$ while close to the junctions there is a remarkable discrepancy.

The efficiency corresponding to the figure of merit and its improved versions is, by construction, the maximal possible efficiency for the applied temperatures. In the simulation we set the electrical current to a fixed value and then determine the corresponding efficiency. To determine the electrical current for which the efficiency shows a maximum, we perform several simulations with different currents j and estimate from the corresponding efficiencies the current j_m that gives the maximum efficiency. Then we do another simulation with this current to get the exact numerical value for the performance. The efficiency simulations have been done with n-doped Bi_2Te_3 in region 2 and transport coefficients of a metal in region 4. This means that we are left with an effective one-leg thermoelectric generator. The reason for this is that the engineering figure of merit has only been defined for a one-leg device. Furthermore this treatment makes it easier to understand the different effects as they only stem from one material. The other simulation parameters are the same as above except for the length which is $l = l_{ex} = 1mm$, a realistic order of magnitude. The results of the $1mm$ calculations are

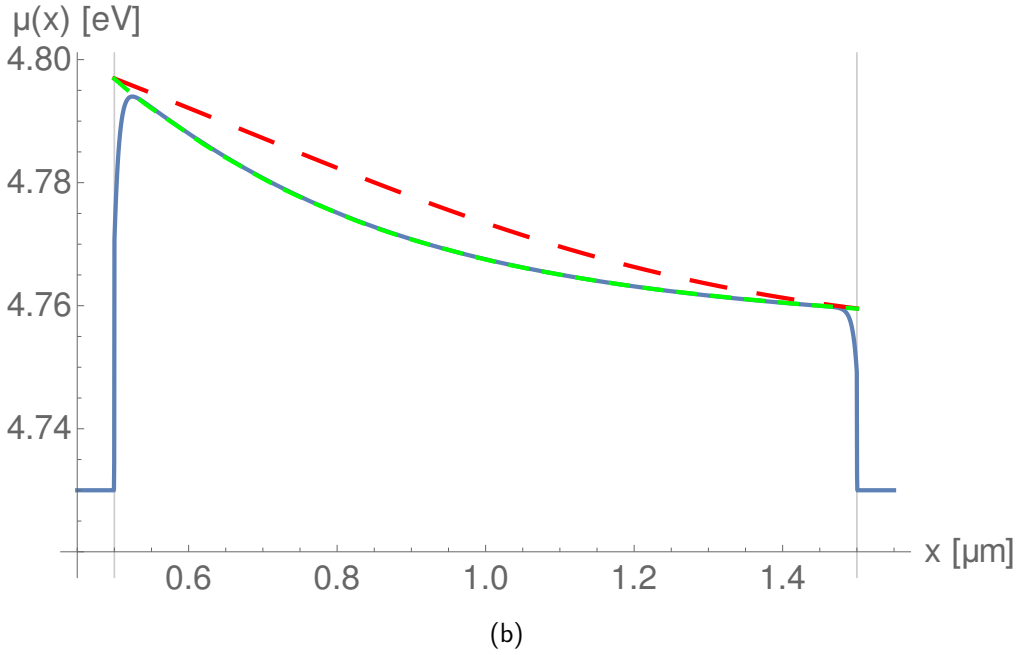
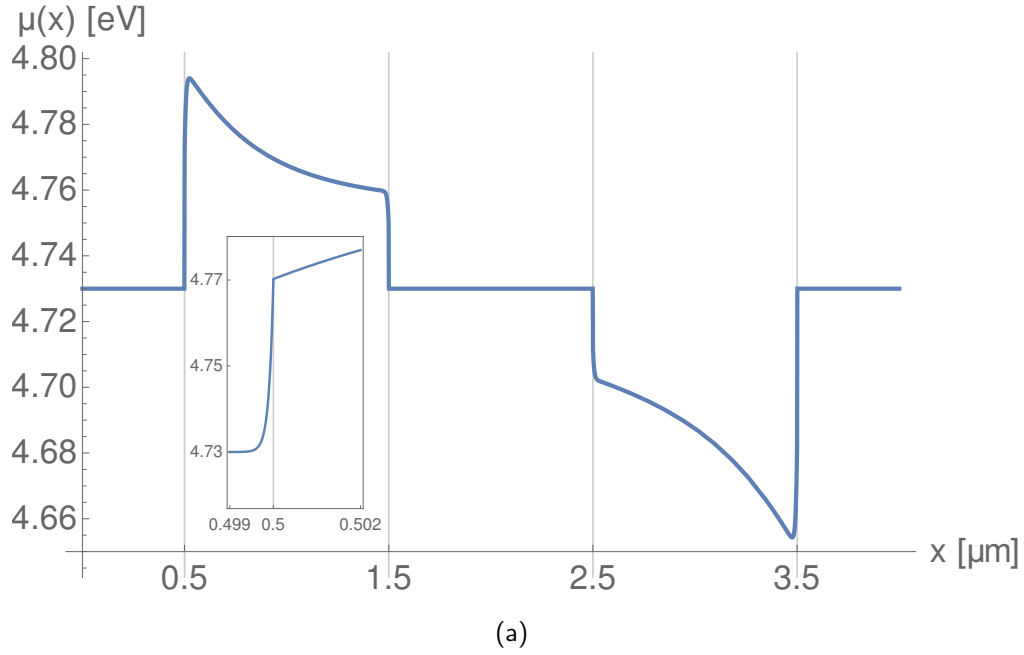


Figure 5.1.: Chemical potential for a device composed of n-doped Bi_2Te_3 for region 2 (from $x = 0.5\mu\text{m}$ to $x = 1.5\mu\text{m}$) and p-doped for region 4 (from $x = 2.5\mu\text{m}$ to $x = 3.5\mu\text{m}$). Panel (a) shows the chemical potential distribution across the whole device. The inset is a zoom around $x = 0.5$ and emphasizes the fact that the chemical potential is continuous and deviates from the Fermi-energy also within the metal ($x < 0.5$). The second plot (b) shows $\mu(x)$ in region 2 (blue), the equilibrium chemical potential assuming a linear temperature slope (red, dashed) and the equilibrium chemical potential for the calculated temperature distribution (green, dashed).

| | $T_0 = 300 \ T_l = 600$ | $T_0 = 300 \ T_l = 301$ |
|--------------------------------------|-------------------------|-------------------------|
| $\eta(Z_{\text{av-1}}T_m)$ | 3.27% | 0.0252% |
| $\eta(Z_{\text{av-2}}T_m)$ | 3.63% | 0.0252% |
| $\eta_{\text{eng}}(ZT_{\text{eng}})$ | 2.81% | 0.0252% |
| η_{sim} | 2.98% | 0.0251% |

Here, we can see that the two averaged figures of merit (see equations (2.36) and (2.37)) slightly overestimate the efficiency while the engineering figure of merit (equation (2.38)) gives a smaller value. The reason for the difference between the simulation and the engineering figure of merit purely stems from the non-linear temperature distribution. As can be seen in figure 5.1 the equilibrium chemical potential for a linear temperature profile is different from the equilibrium chemical potential for the real temperature distribution. The engineering figure of merit uses the transport coefficients at the equilibrium chemical potential for an assumed linear $T(x)$. Hence, the efficiency differs from the simulation. The non-linear temperature distribution is due to the strongly temperature dependent thermal conductivity κ . In principle the Joule and Thomson heating can also lead to a deviation of the temperature profile from a linear behavior. However, in this case they do not play an important role as can be inferred by noticing that the temperature distribution is only marginally affected by the current running through the device (figure 5.2(b)).

The current induced distortion of the chemical potential is negligible (figure 5.2(a)) and $\mu(x)$ is almost at its equilibrium value $\mu_{\text{eq}}(T_2(x))$ (figure 5.1(b)). Therefore we can be sure that the difference in the efficiencies does not stem from explicit chemical potential distortions.

In case of small temperature differences the four efficiencies become equal which is required by consistency.

We can conclude that for Bi_2Te_3 the engineering figure of merit gives the best agreement with the efficiency obtained by simulation. The small deviation is due to the fact that the engineering figure of merit assumes a linear temperature slope rather than the real temperature distribution. The explicit treatment of the chemical potential has little influence on the efficiency in this example. However, we will see that there can be severe differences in other materials as I will discuss for SrTiO_3 .

5.1.1. Optimization

As explained in section 4.3 we have implemented an optimization routine for the doping level. This routine is capable of calculating the optimum uniform doping level as well as the optimum doping distribution. In the latter case the doping is varied at n different points which gives rise to an n -dimensional optimization problem. In a first step we calculate the optimum uniform doping. For that purpose we apply the algorithm to the n -doped Bi_2Te_3 we have already used before. The

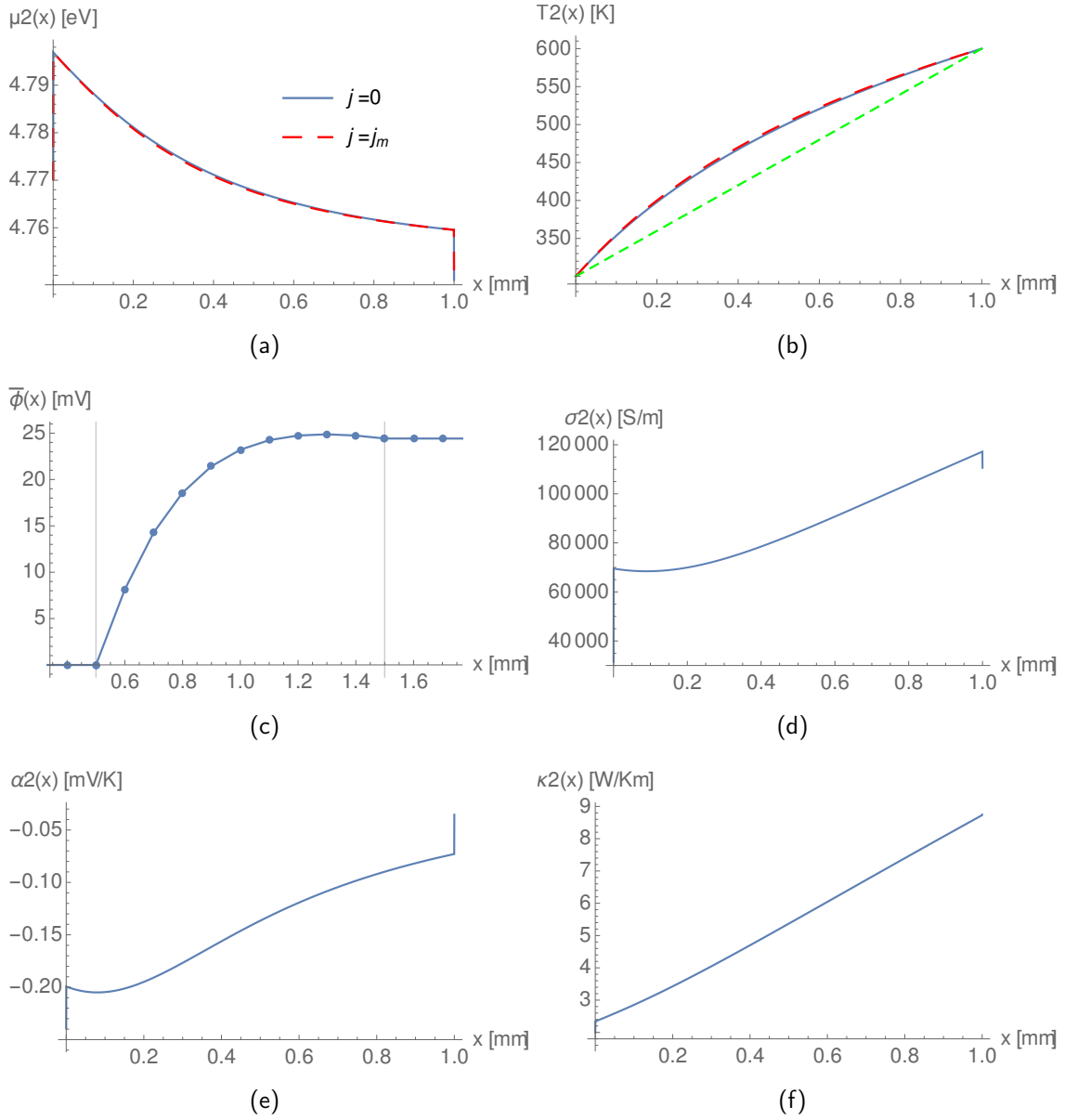


Figure 5.2.: Different quantities calculated for Bi_2Te_3 at the current j_m that gives the maximum efficiency. The chemical potential for $j = j_m$ is almost the same as for $j = 0$ (a) as well as the temperature distribution (b). The green line in (b) is a linear slope which would be the correct temperature distribution for zero current and constant transport coefficients. As explained in the text the non-linear temperature profile stems from the non-linear thermal conductivity κ . Figure (b) shows the electrochemical potential distribution. The shape is determined by the Seebeck effect and the voltage loss due to the internal resistance. The transport coefficients in dependence of the position are also given for completeness (d)-(f). The seeming discontinuity at the outermost points are merely sharp bends and stem from the chemical potential distortion at the junctions.

device parameters are the same as in the initial example at the beginning of this chapter. The lengths of the device legs are $l = l_{\text{ex}} = 2\mu\text{m}$ as above which reduces the computational demand. However, the results can be extended to systems of realistic size as verified at the end of this section.

The optimization routine optimizes the efficiency at a fixed current. We know that the optimal current j_m depends on the properties of the material, hence, the current for which the optimization was done is not the optimal current for the newly doped system. Therefore the new optimal current \tilde{j}_m must be calculated for the new doping level. Then the optimization routine must be restarted with the new current, and so on until the doping does not change within the specified tolerance.

This iteration yields an optimal uniform doping level which is $d = 1.6476 * 10^{25}\text{m}^{-3}$ with a corresponding efficiency of $\eta = 4.935\%$ for Bi_2Te_3 . Starting from this level we employ the optimization routine with a five-dimensional parameter space. This means that on top of the optimal uniform doping level the program searches for a non-uniform doping distribution relative to the current one that further increases the efficiency. We find that the doping distribution shown in figure 5.3 increases the efficiency to a value of $\eta = 5.596\%$. This is an increase of 0.661 percent points or a relative increase by 13.4%.

In addition to the calculated doping distribution we also studied the behavior of the ordinary figure of merit for different temperatures and doping levels. We find that for a certain temperature T the figure of merit shows a maximum for a certain uniform doping level $d_m(T)$. In figure 5.3 we show this plot in dependence of the calculated temperature $T_2(x)$, i.e. $d_m(T_2(x))$ (green, dashed). Surprisingly the numerically calculated optimum doping concentration is in fairly good agreement with the green, dashed line that only follows the maximum of the ordinary figure of merit. The efficiency for this doping distribution is $\eta = 5.543\%$ which is almost the same as for the optimized doping. Note that this correlation does not need to be true for different materials.

To verify that the doping distributions are applicable to larger devices as well, we calculate the efficiencies for the uniform and the non-uniform case for a device with $l = l_{\text{ex}} = 1\text{mm}$. The non-uniform distribution has been scaled to the new length. We find that the efficiency is $\eta = 4.935\%$ for uniform doping and $\eta = 5.581\%$ for the scaled non-uniform doping. This indicates that the efficiency of Bi_2Te_3 is almost independent of the actual leg-size and therefore the doping distribution is also the optimum for the larger device.

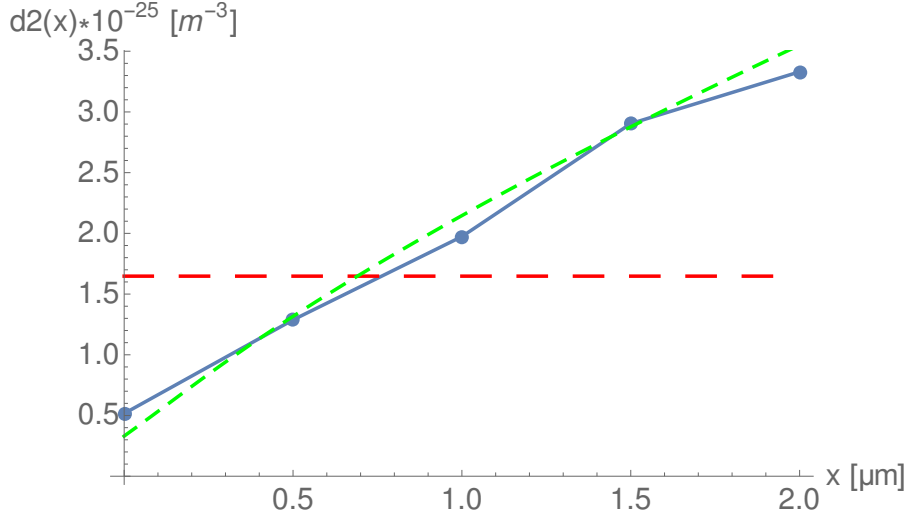


Figure 5.3.: Optimum uniform doping (dashed, red) and non-uniform doping (blue). The efficiency for uniform doping is $\eta = 4.935\%$ and $\eta = 5.596\%$ for the non-uniform case. The dashed, green line shows the doping for which the ordinary figure of merit would be the maximum for the calculated temperature distribution $T_2(x)$. The efficiency for this case is $\eta = 5.543\%$ which is almost identical with the efficiency of the optimized doping.

5.2. SrTiO_3

Strontium titanate is a perovskite-type transition-metal oxide. In its pure state it is an insulator with a band-gap of about 3.25eV [27]. However, it can be doped with rare earths in order to bring the chemical potential up to the edge of the conduction band. This makes SrTiO_3 an admirable thermoelectric with a power factor comparable to bismuth telluride [28]. Even when the efficiency is worse due to the higher lattice thermal conductivity it is an interesting candidate for high temperature thermoelectric generators due to its high melting point of $T_m = 2080\text{K}$ [29].

We have performed the WIEN2K-DFT simulation of the band structure [14, 16–20, 30] and then obtained the transport properties using BoltrTraP [21]. For the unit cell volume we use $V_{\text{uc}} = 5.95 * 10^{-29}\text{m}^3$ [28] and for the relaxation time $\tau = 0.43 * 10^{-14}\text{s}$ [31]. We discuss n-doped SrTiO_3 where we apply a doping concentration of

$$d_n = 5 * 10^{26}\text{m}^{-3} \quad (5.3)$$

for which the calculated Seebeck coefficient and electronic conductivity are in reasonable agreement with the experimentally measured values of similarly doped strontium titanate [28]. We choose the phononic part of the thermal conductivity as $\kappa_{ph} \approx 4\text{Wm}^{-1}\text{K}^{-1}$ in order to restore the correct order of magnitude [28]. The

static dielectric constant is obtained from a Curie-Weiss fit at room temperature and yields $\epsilon \approx 288$ [32]. The temperatures we use are $T_0 = 400K$ and $T_l = 700K$ and the equilibrium chemical potentials of the metals are $\mu_{\text{eq-}i} = 8eV$ $i \in \{1, 3\}$. The lengths of the device legs are $l = l_{\text{ex}} = 1mm$. From the DFT calculations of SrTiO_3 we find the bottom of the conduction band at $\epsilon_{\text{cond}} = 8.1eV$.

For the differently obtained efficiencies we find

| | $T_0 = 400 \ T_l = 700$ |
|--------------------------------------|-------------------------|
| $\eta(Z_{\text{av-1}}T_m)$ | 2.58% |
| $\eta(Z_{\text{av-2}}T_m)$ | 2.53% |
| $\eta_{\text{eng}}(ZT_{\text{eng}})$ | 2.52% |
| η_{sim} | 2.52% |

In contrast to the previously discussed case of Bi_2Te_3 all three versions of the figure of merit are in very good agreement with the simulation. The reason is that the transport coefficients change almost linearly with temperature (figures 5.4(d)-5.4(f)) which makes the averaged figures of merit a good approximation. The temperature profile is close to a linear slope as the (constant) phononic heat conductivity contribution is larger than the electronic part. As for bismuth telluride the chemical potential is hardly affected by the electrical current (figure 5.4(a))

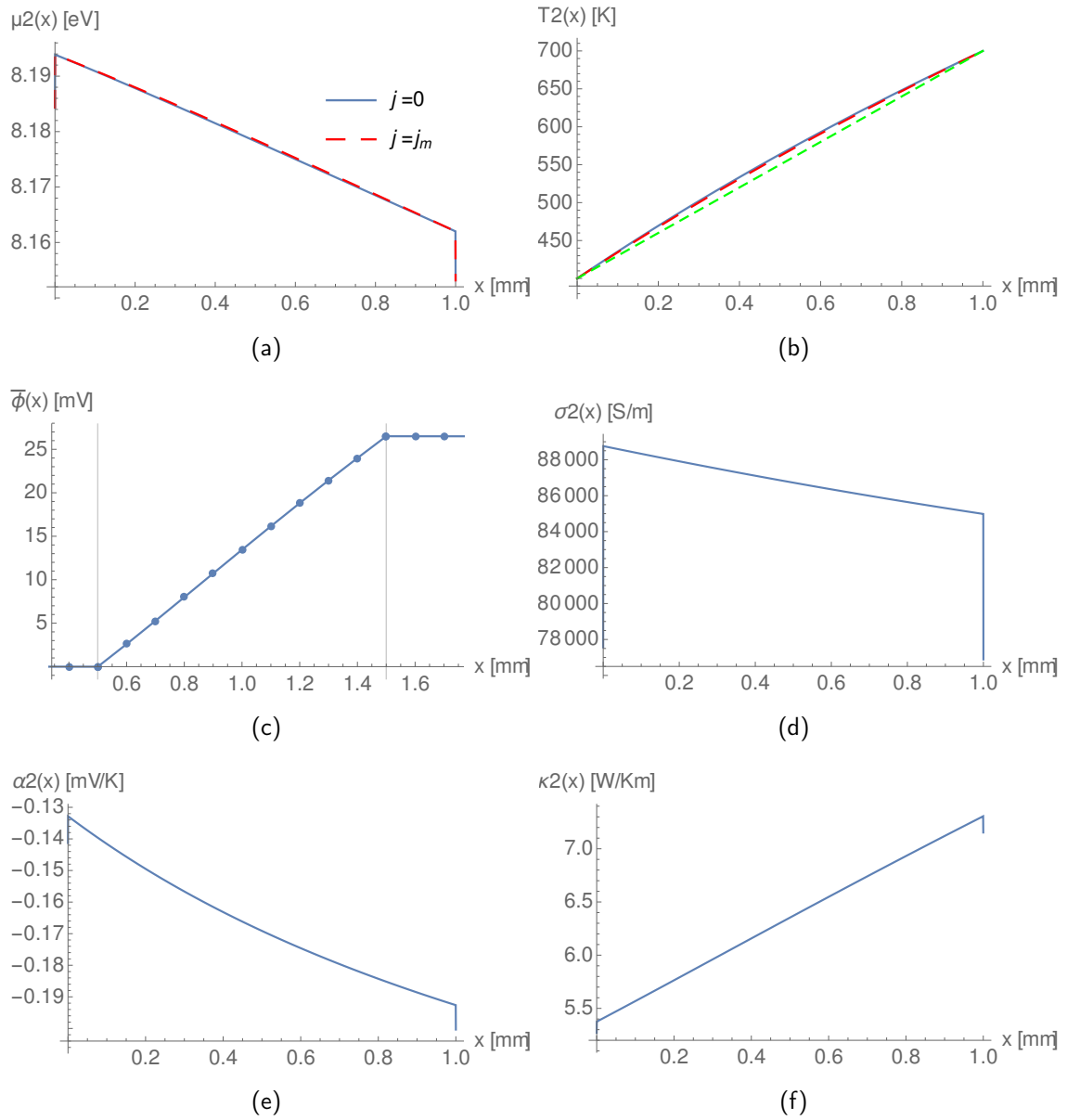


Figure 5.4.: Same as figure 5.2 but for SrTiO_3 .

Although the figures of merit are in almost perfect agreement with the simulation given in the example above, there are cases when the simulated efficiency dramatically deviates from the predicted values. This happens for certain equilibrium chemical potentials ($\mu_{\text{eq-i}}$) and decay lengths (ξ_i) of the metallic contacts. The efficiencies we find for different parameters are

| $T_0 = 400 \text{ K} \quad T_l = 700 \text{ K}$ | $\xi_i = 1 * 10^4 \mu\text{m}^{-1}$ | $\xi_i = 2 * 10^4 \mu\text{m}^{-1}$ | $\xi_i = 3 * 10^4 \mu\text{m}^{-1}$ |
|--|-------------------------------------|-------------------------------------|-------------------------------------|
| $\mu_{\text{eq-i}} - \epsilon_{\text{cond}} = -0.1 \text{ eV}$ | 2.518% | 2.518% | 2.518% |
| $\mu_{\text{eq-i}} - \epsilon_{\text{cond}} = -1.1 \text{ eV}$ | 2.518% | 2.518% | 2.518% |
| $\mu_{\text{eq-i}} - \epsilon_{\text{cond}} = -2.1 \text{ eV}$ | 2.518% | 2.516% | 1.848% |

where the three decay lengths correspond to the three following densities of states:

$$\xi_i = 1 * 10^4 \mu\text{m}^{-1} \rightarrow N(\epsilon_f) = 0.345 * 10^{47} \text{ J}^{-1} \text{ m}^{-3}, \quad (5.4a)$$

$$\xi_i = 2 * 10^4 \mu\text{m}^{-1} \rightarrow N(\epsilon_f) = 1.380 * 10^{47} \text{ J}^{-1} \text{ m}^{-3}, \quad (5.4b)$$

$$\xi_i = 3 * 10^4 \mu\text{m}^{-1} \rightarrow N(\epsilon_f) = 3.105 * 10^{47} \text{ J}^{-1} \text{ m}^{-3}. \quad (5.4c)$$

The efficiencies for $\mu_{\text{eq-i}} - \mu_{\text{cond}} = -2 \text{ eV}$ depend on the decay length of the attached metals while they are independent of the decay length for higher chemical potential values. We can identify the so-called Schottky effect [33] as the reason for this behavior. This effect describes the drop in the electrochemical potential at metal-semiconductor junctions. When a metal and a (doped) semiconductor are brought into electrical contact their chemical potentials align as electrons diffuse from the material with the higher equilibrium chemical potential into the material with the lower one. This distortion of the chemical potential affects the transport coefficients, especially if the chemical potential of the semiconductor is forced to cross its band gap. If this is happening the electrical conductivity can drop dramatically which creates an insulating layer at the junction (figures 5.5(c), 5.5(d)). When an electrical current is driven through the device that layer generates an additional electrochemical potential drop. This is the cause of the strong reduction in the efficiency for the strontium titanate in the simulations shown in the last row of the table above. The output voltage ($U = \bar{\phi}(2l + 2l_{\text{ex}}) - \bar{\phi}(0)$) is reduced by the loss at the junction which, in turn, decreases the efficiency (figures 5.5(e), 5.5(f)).

In most cases the chemical potential of the semiconductor is forced to the equilibrium value of the metal as the latter has a much higher free charge carrier concentration. For SrTiO_3 this is not necessarily true as it needs a high doping concentration to bring the chemical potential up to the band-edge where the figure of merit is the highest. Note that in our model the doping concentration is equal to the charge carrier concentration. Therefore the chemical potential of the strontium titanate tends to stay close to the equilibrium value while the chemical potential of the attached metal is driven away in case the metal density of states at the Fermi level

(which corresponds to ξ_i according to equation (3.30)) is too low (see figures 5.5(a), 5.5(b)).

The electrical conductivities given by the figures 5.5(c), 5.5(d) show that there is a conductivity drop for all three values of ξ_i while the corresponding electrochemical potentials only show an effect for the highest ξ_i . This can be understood with the different resistances of the insulating areas. Only when the total resistance of the badly conducting layer (which is proportional to its thickness and which depends exponentially on the position of the chemical potential) becomes comparable to the resistance of the rest of the device, the voltage loss is strong enough to become important.

We can conclude that the explicit inclusion of the chemical potential in the simulation leads to qualitative and quantitative differences for SrTiO_3 . The reason for that is the Schottky effect which cannot be accounted for by simulations which only incorporate the temperature dependence of the transport properties. However, the effect might not be seen in experiments as doped strontium titanate has a high charge carrier concentration which counteracts the distortion of the chemical potential at the junction.

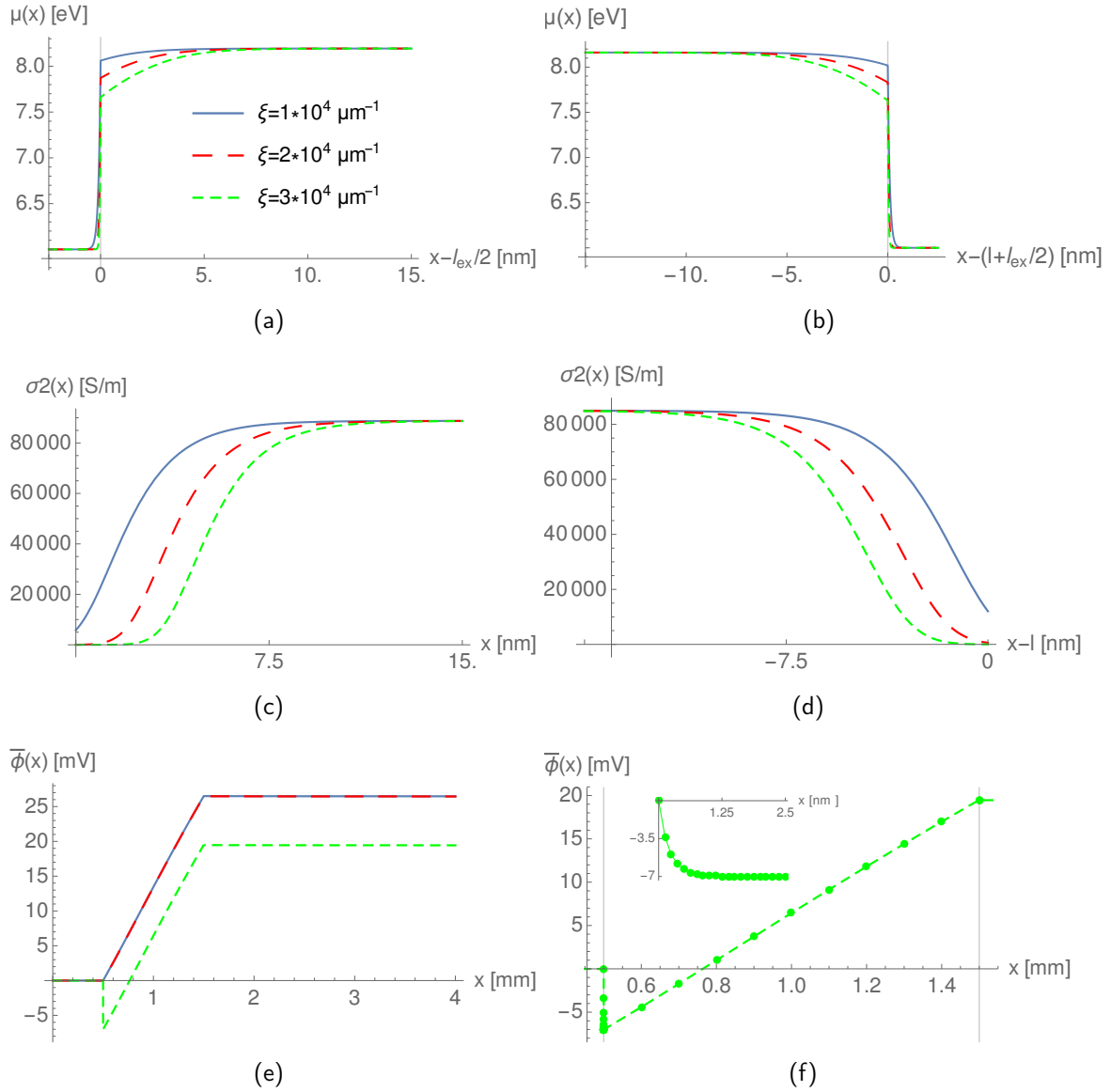


Figure 5.5.: The chemical potential ((a),(b)) and the electrical conductivity ((c),(d)) at the junctions for different decay lengths ξ_i of the attached metals. The equilibrium chemical potential of the metals is $\mu_{eq-i} = 6eV$ (the conduction band starts from $\epsilon_{cond} = 8.1eV$). We see that the electrical conductivities are dramatically decreased at the junctions ((c),(d)). For the case $\xi_i = 3 \times 10^4 \mu m^{-1}$ we observe a drop in the electrochemical potential at the left junction (e). This happens when the resistance of the badly conducting junction-area becomes comparable to the total resistance of the rest of the device. The drop is not discontinuous but very sharp which is shown by figure (f) where the dots mark the calculated points.

5.3. FeSb_2

The correlated inter-metallic compound FeSb_2 has attracted attention recently as it exhibits a uniquely high power-factor at low temperatures [7]. It shows a narrow band-gap of about several meV depending on the temperature [7]. The mechanism behind colossal Seebeck coefficient could be identified as in-gap states which couple to phonons [6]. Although the power-factor of FeSb_2 is enormous (about 65 times larger than Bi_2Te_3) the figure of merit and therefore the efficiency as well, are rather moderate due to the large thermal conductivity. The transport coefficients we use were not calculated from a real band-structure but from a model density of states which takes into account the narrow in-gap bands and the phonon-drag effect. The details can be found in Ref. [6]. The major part of the heat conductivity at low temperatures stems from the lattice contribution and was taken from Ref. [7]. For the dielectric constant we use $\epsilon = 30$ [34] and the lengths of the device legs are $l = l_{\text{ex}} = 1\text{mm}$.

For the different efficiencies we find

| | $T_0 = 5 \text{ } T_l = 25$ |
|--------------------------------------|-----------------------------|
| $\eta(Z_{\text{av-1}}T_m)$ | 0.0275% |
| $\eta(Z_{\text{av-2}}T_m)$ | 0.0222% |
| $\eta_{\text{eng}}(ZT_{\text{eng}})$ | 0.0144% |
| η_{sim} | 0.0169% |

The averaged figures of merit overestimate the efficiency even more than for Bi_2Te_3 as the transport coefficients of FeSb_2 are highly non-linear (figures 5.6(d)-5.6(f)). Again the engineering figure of merit is in much better agreement with the simulation but also slightly underestimates the efficiency. As for bismuth telluride this can be explained with the influence that the temperature has on the position of the equilibrium chemical potential.

We can conclude that although FeSb_2 has highly non-linear transport properties the engineering figure of merit gives a very precise estimation of the real efficiency. This is due to the fact the non-linearities mainly stem from the locally different temperature which is also taken into account to some extent by the engineering figure of merit. The explicit treatment of the chemical potential does not uncover any unexpected features in contrast to SrTiO_3 .

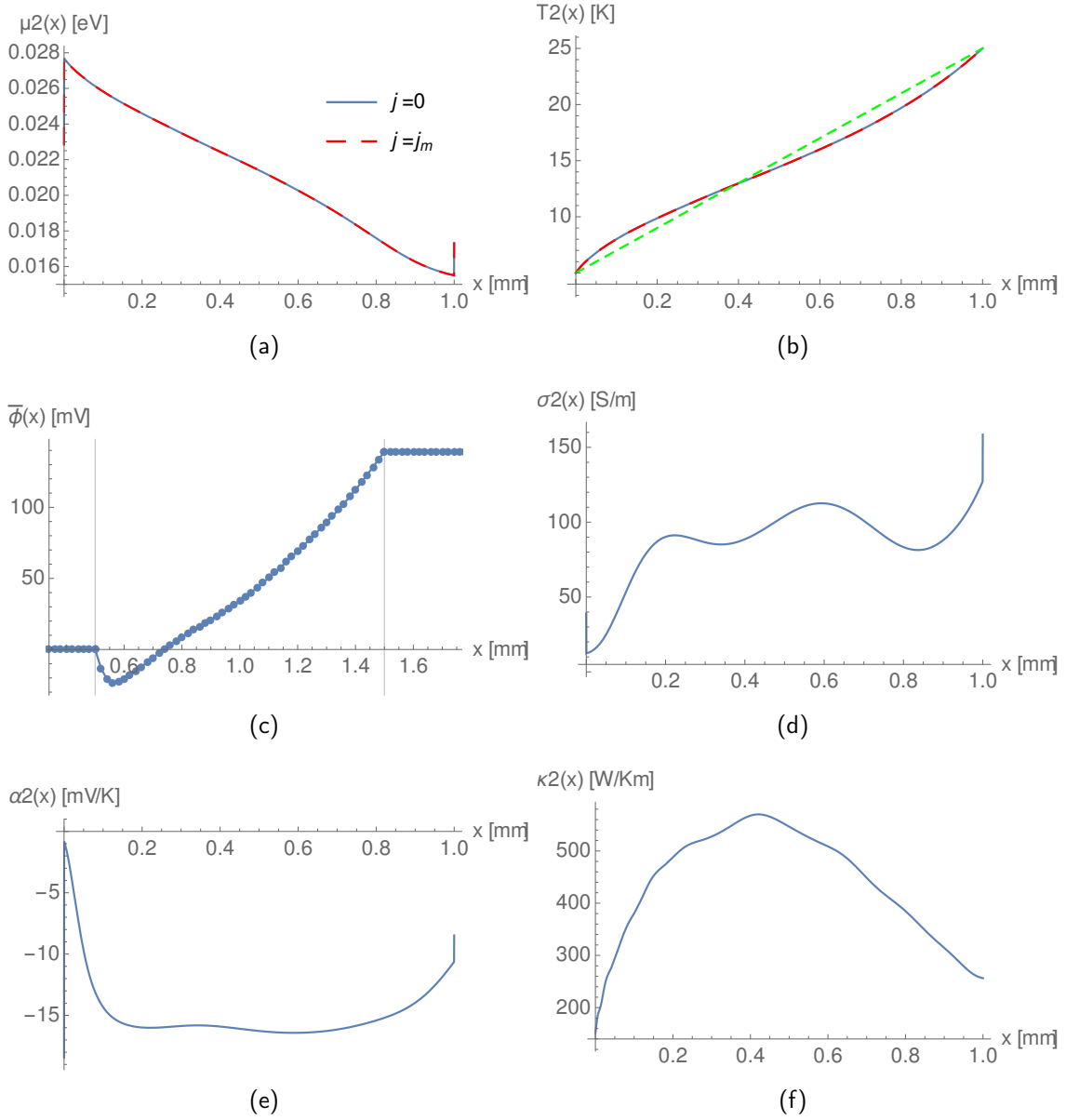


Figure 5.6.: Same as figure 5.2 but for FeSb_2 . The negative slope at the left junction stems from the voltage loss due to the low electrical conductivity and a poor Seebeck coefficient at $T = 5\text{K}$.

6. Conclusion

In this work we have applied the macroscopic transport equations to a two-leg thermoelectric device including the full dependence of the transport properties on the temperature as well as on the chemical potential. We have derived general boundary conditions for junctions between different materials and applied them to a simplified model system. In order to solve the non-linear, coupled differential equations a numerical solver was built which eventually gives the actual temperature- and chemical potential distributions $T(x)$ and $\mu(x)$ for the operating point of the device. We describe the metallic leads of the device by constant transport coefficients but take distortions of the chemical potential into account. After the program has calculated $T(x)$ and $\mu(x)$ the corresponding efficiency can be determined.

In order to check if the explicit treatment of the chemical potential leads to significant differences we have simulated Bi_2Te_3 , SrTiO_3 and FeSb_2 and compared the efficiencies to the values the different figures of merit propose, including the recently introduced engineering figure of merit. We find that in most cases the simulation is in good agreement with the engineering figure of merit and the small differences mainly emerge from the non-linear temperature distribution that is established in the real device.

However, the attached metals can strongly distort the chemical potential in the active material. In some specific cases an insulating layer at the junction is generated. This layer can be large enough that the voltage loss due to its poor conductivity is comparable to the loss in the rest of the device which can dramatically reduce the efficiency. This junction effect is known as Schottky-contact and has always been neglected so far in thermoelectric simulations. The size of the effect is determined by the gap-size of the active material but also by the density-of-states and the equilibrium chemical potential of the attached metal. Interestingly in the studied materials the effect does not play a role or, in case of the SrTiO_3 , it does only for specific parameters of the attached metal. This may be the case why this effect has always been neglected in this context hitherto. However, this does not exclude that this effect might have led to the discard of theoretically promising materials which proved to perform below the expectations experimentally.

Additionally we have implemented a routine that calculates the optimum doping distribution along the active material. For bismuth telluride we find that the efficiency can be increased by $\approx 13\%$ by a non-uniform doping profile compared to uniform doping.

A. Program

The simulation program needs several input parameters which define the system geometry (figure 4.1) and the materials in the four different regions. The program requires the transport coefficients and the charge density in dependence of the chemical potential (in eV) and the temperature (in K) for regions 2 and 4 as files in the *Mathematica-WDX* format. The program assumes that the first argument is the temperature and the second one is the chemical potential. Furthermore the program needs the equilibrium chemical potential in dependence of the temperature. The files containing the data have to have specific names which are defined as

| quantity | unit | description | filename |
|------------------|-----------|--------------------------------|---------------|
| $\rho_f[T, \mu]$ | Cm^{-3} | charge density | charge.dat |
| $\sigma[T, \mu]$ | Sm^{-1} | electrical conductivity | conduct.dat |
| $\alpha[T, \mu]$ | VK^{-1} | Seebeck coefficient | seebeck.dat |
| $\kappa[T, \mu]$ | WK^{-1} | thermal conductivity | thermcond.dat |
| $\mu_{eq}[T]$ | eV | equilibrium chemical potential | chemequil.dat |

and have to be located in the same directory. As the program needs precise equilibrium chemical potential values it calculates them on its own and the distribution given by *chemequil.dat* is only taken as starting point for finding the correct value. The user is supposed to use the program via the provided graphical user interface (GUI) which can be started by executing the function *widget[]*. There is an input mask for all the necessary input parameters that are needed which are

| quantity | unit | description |
|-------------------------------|------------|--|
| T_0 | K | temperature at the left side of the device |
| T_l | K | temperature at the right side of the device |
| l | μm | length of the regions 2 and 4 |
| l_{ex} | μm | length of the regions 1 and 3 |
| l_{dep} | μm | size of the regions with the grid point number n_{dep} (see equation (4.31)) |
| j | Amm^{-2} | electrical current density |
| $\mu_{\text{eq } 1/3}$ | eV | equilibrium chemical potential of the metal in region 1/3 |
| $\sigma_{1/3}$ | Sm^{-1} | electrical conductivity in region 1/3 |
| $\xi_{1/3}$ | m^{-1} | decay length according to equation (3.30) in region 1/3 |
| n_l | 1 | number of points within $l_{\text{dep}} \leq x < l - l_{\text{dep}}$ for regions 2/4 |
| n_{dep} | 1 | number of points in each of the intervals $0 \leq x < l_{\text{dep}}$ and $l - l_{\text{dep}} \leq x < l$ |
| <i>max runs</i> | 1 | maximum number of iteration cycles |
| <i>T - res</i> | K | termination value which determines when the temperature iteration is converged |
| <i>μ - res</i> | eV | termination value which determines when the chemical potential iteration is converged |
| <i>output mesh</i> | μm | point spacing for <i>exportdata</i> routine |
| <i>ϕmesh</i> | μm | point spacing for the electrochemical potential |
| $\delta_{2/4}$ | 1 | mixing parameter for the iteration cycle |
| $\epsilon_{2/4}$ | 1 | relative permittivity of region 2/4 |
| <i>size</i> | 1 | changes the size of the displayed plots; a new value has to be acknowledged by pressing the return-button |

The figure A.1 shows the graphical user interface where different regions are labeled with the letters *a-f*. In the section *a* one can enter the paths of the directories where the files with the transport properties for the areas 2 and 4 are located. The third mask is for the output path which is the directory in which the files are saved when the *export data* routine is executed. The section *b* shows the input fields for the parameters given by the table above. With the drop down menu one can decide whether the heat currents through both legs of the device shall be taken into account for the efficiency calculation or just one which then is the area 2 in particular. This makes sense when one wants to study only one material which can be achieved by using a material with zero Seebeck coefficient for region 4 and the *single j_Q* - option. The region *f* gives status informations on the current simulation and in the end of one simulation the calculated efficiency is displayed here as well. The program is controlled by the buttons in region *c* which are explained by the table below. In the region *d* the program plots some of the important quantities such as the chemical potential or the temperature distribution after the calculation

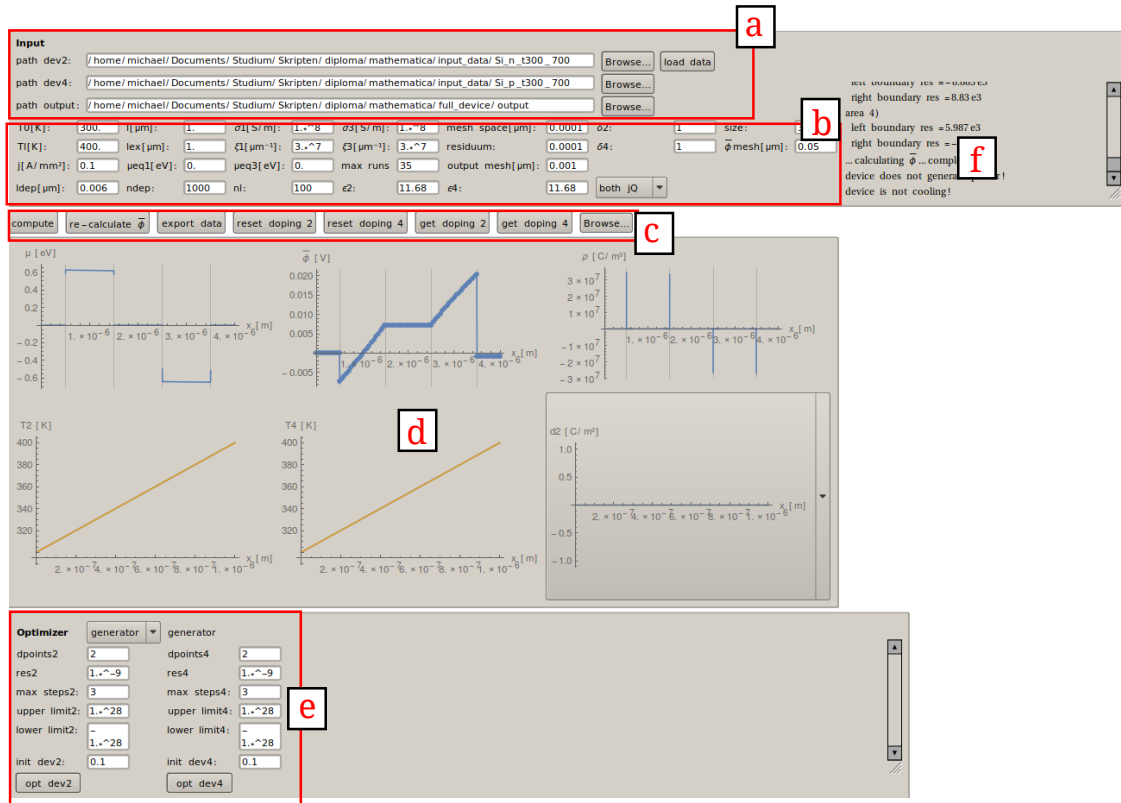


Figure A.1.: Picture of the graphical user interface.

has finished. The area *e* is for the optimization routine which is explained in detail in section A.2.

| button name | function |
|---------------------------|--|
| compute | starts a calculation with the current parameters |
| re-calculate $\bar{\phi}$ | calculates only $\bar{\phi}$ |
| export data | saves the quantities $\mu(x)$, $\mu_{2/4}(x)$, $T_{2/4}(x)$, $\rho(x)$, $\sigma_{2/4}(x)$, $\alpha_{2/4}(x)$ and $\bar{\phi}(x)$ as tables or Mathematica-definitions; the coefficients a_i/b_i are saved in the file <i>analytical.dat</i> some of the input parameters are saved in <i>info.dat</i> |
| reset doping 2/4 | sets the doping function of area 2/4 to zero |
| get doping 2/4 | imports a previously saved doping function; the location is the one specified with the <i>browse</i> button |
| browse | specifies the location of the directory for the <i>get doping2/4</i> routines |

A.1. Starting a simulation

The first step is to start the graphical user interface by executing the function `widget[]`. Then one has to set the paths of the directories where the necessary input files are located with the *Browse...* buttons (region *a* in figure A.1). Note that both input paths may be the same which would mean that the program uses the same transport properties for the regions 2 and 4. Then the input files have to be loaded with the *load data* button. The success or failure of the loading process is reported in the information panel (region *f*). Then one has to enter the input parameters (region *b*) where one has to be careful whether the temperature- and equilibrium chemical potential-ranges are covered by the loaded transport property - files. If not the program extrapolates which may lead to wrong or unphysical results. After all parameters are set the simulation is started with the *compute* button (region *c*).

If everything worked the efficiency of the device and its output power in case of a generator are displayed in the information panel and the calculated quantities are plotted (region *d*).

A.2. Optimization routine

The optimization routine calculates the doping function $d_i(x)$ (see section 4.3) for which the efficiency approaches a maximum. With the drop down menu one can select whether the device has to be optimized for power generation or for cooling. Usually only one of these options works for a specific parameter set as the device is either cooling or generating power. As explained in section 4.3 the doping function is only varied on some points and the continuous function is then calculated by linear interpolation. The input parameter $dpoints_i$ specifies the number of these points which is equal to the dimension of the optimization problem. A value of 1 would mean that the doping function is a constant which can be used to find the optimal uniform doping level. For a value of 2 the doping function values at the boundaries are used ($d_i(0)$ and $d_i(l)$) and for higher $dpoints_i$ -values additional points are added between so that the resulting intervals are equidistant. The input parameter res_i is the test for the convergence which means that the optimization stops when $\Delta < res_i$ where Δ is defined by equation (4.39). The *max steps* parameter stands for the maximum number of iteration cycles after which the optimization routine is stopped regardless of convergence. Since not every arbitrary doping level can be achieved physically one can restrict the doping function to a certain interval which is specified by the parameters *upper limit* and *lower limit*. The last input parameter is *init dev_i* which is needed for the initial points. As explained in section 4.3 the used Nelder-Mead algorithm needs $dpoints_i + 1$ initial points in the $dpoints_i$ -dimensional optimization space. The first of these points is generated by setting

all doping function points to zero while the other points are generated by letting all doping function points be zero except one. At this point the doping function is given the value that would shift the equilibrium chemical potential by a factor of $init\ dev_i$.

Bibliography

- [1] L. E. Bell. *Cooling, Heating, Generating Power, and Recovering Waste Heat with Thermoelectric Systems*. SCIENCE **321** (2008).
- [2] S. LeBlanc. *Thermoelectric generators: Linking material properties and systems engineering for waste heat recovery applications*. Sustainable Materials and Technologies 1-2 pp. 26–35 (2014).
- [3] X. Zhang and L.-D. Zhao. *Thermoelectric materials: Energy conversion between heat and electricity*. Journal of Materiomics 1 pp. 92–105 (2015).
- [4] G. D. Mahan. *Density variations in thermoelectrics*. Journal of Applied Physics **87**, 7326 (2000).
- [5] G. D. Mahan. *Inhomogeneous thermoelectrics*. Journal of Applied Physics **70**, 4551 (1991).
- [6] M. Battiato, J. M. Tomczak, Z. Zhong, and K. Held. *Unified Picture for the Colossal Thermopower Compound FeSb₂*. Physical Review Letters **114** (2015).
- [7] A. Bentien, S. Johnsen, G. K. H. Madsen, B. B. Iversen, and F. Steglich. *Colossal Seebeck coefficient in strongly correlated semiconductor FeSb₂*. EPL **80** (2007).
- [8] S. H. Kim, W. Liu, G. Chen, C.-W. Chu, and Z. Ren. *Relationship between thermoelectric figure of merit and energy conversion efficiency*. PNAS **112**, 8205 (2015).
- [9] V. Zlatić and R. Monnier. *Modern Theory of Thermoelectricity* (2014).
- [10] L. Onsager. *Reciprocal Relations in Irreversible Processes. I*. Physical Review **37** (1931).
- [11] C. A. Domenicali. *Irreversible Thermodynamics of Thermoelectricity*. Reviews of modern Physics **26** (1954).
- [12] W. Thomson. *4. On a Mechanical Theory of Thermo-Electric Currents*. Proceedings of the Royal Society of Edinburgh **3**, 91 (1857).
- [13] M. Wais. *Numerical solution of the macroscopic transport equations*.

- [14] P. Blaha, K. Schwarz, G. K. H. Madsen, D. Kvasnicka, and J. Luitz. *WIEN2K, An Augmented Plane Wave + Local Orbitals Program for Calculating Crystal Properties*. Karlheinz Schwarz, Techn. Universität Wien, Austria (2001).
- [15] I.-K. Suh, H. Ohta, and Y. Waseda. *High-temperature thermal expansion of six metallic elements measured by dilatation method and X-ray diffraction Locality: synthetic Sample: at $T = 1076$ K*. Journal of Materials Science **23**, 757 (1988).
- [16] A. Merkys, A. Vaitkus, J. Butkus, M. Okulič-Kazarinas, V. Kairys, and S. Gražulis. *COD::CIF::Parser: an error-correcting CIF parser for the Perl language*. Journal of Applied Crystallography **49** (2016).
- [17] S. Gražulis, A. Merkys, A. Vaitkus, and M. Okulič-Kazarinas. *Computing stoichiometric molecular composition from crystal structures*. Journal of Applied Crystallography **48**, 85 (2015).
- [18] S. Gražulis, A. Daškevič, A. and Merkys, D. Chateigner, L. Lutterotti, M. Quirós, N. R. Serebryanaya, P. Moeck, R. T. Downs, and A. LeBail. *Crystallography Open Database (COD): an open-access collection of crystal structures and platform for world-wide collaboration*. Nucleic Acids Research **40** (2012).
- [19] S. Gražulis, D. Chateigner, R. T. Downs, A. T. Yokochi, M. Quirós, L. Lutterotti, E. Manakova, J. Butkus, P. Moeck, and A. LeBail. *Crystallography Open Database - an open-access collection of crystal structures*. Journal of Applied Crystallography **42**, 726 (2009).
- [20] R. T. Downs and M. Hall-Wallace. *The American Mineralogist Crystal Structure Database*. American Mineralogist **88**, 247 (2003).
- [21] G. K. H. Madsen and D. J. Singh. *BoltzTraP. A code for calculating band-structure dependent quantities*. Computer Physics Communications **175**, 67 (2006).
- [22] J. A. Nelder and R. Mead. *A Simplex Method for Function Minimization*. The Computer Journal **7**, 308 (1965).
- [23] T. J. Scheidemantel, C. Ambrosch-Draxl, and T. Thonhauser. *Transport coefficients from first-principles calculations*. Physical Review B: Condensed Matter and Materials Physics **68** (2003).
- [24] A. H. Li, S. H. Z. Shahbazi, G. X. Wang, C. Zhang, P. Jood, and G. Peleckis. *Electronic structure and thermoelectric properties of Bi_2Te_3 crystals and graphene-doped Bi_2Te_3* . Thin Solid Films **518**, 57 (2010).

- [25] T. E. Svechnikova, L. E. Shelimova, and P. P. Konstantinov. *Thermoelectric Properties of $(\text{Bi}_2\text{Te}_3)_{1-x-y}(\text{Sb}_2\text{Se}_3)\text{Te}_3)_x(\text{Sb}_2\text{Se}_3)_y$ Single Crystals*. Inorganic Materials **41**, 1043 (2005).
- [26] L. I. Berger. *Semiconductor Materials*. CRC Press (1997).
- [27] K. van Benthem, C. Elsässer, and R. H. French. *Bulk electronic structure of SrTiO_3 : Experiment and theory*. Journal of Applied Physics **90**, 6156 (2001).
- [28] M. Hiroaki, K. Kurosaki, and S. Yamanaka. *Thermoelectric properties of rare earth doped SrTiO_3* . Journal of Alloys and Compounds **350**, 292 (2003).
- [29] *SrTiO_3 heat capacity, melting point, density: Datasheet from Landolt-Börnstein - Group III Condensed Matter · Volume 41E: “Ternary Compounds, Organic Semiconductors” in SpringerMaterials (http://dx.doi.org/10.1007/10717201_531)*. Copyright 2000 Springer-Verlag Berlin Heidelberg.
- [30] V. M. Longo, M. das Graca Sampaio Costa, A. Zirpole Simoes, I. L. V. Rosa, C. O. P. Santos, J. Andres, E. Longo, and J. A. Varela. *On the photoluminescence behavior of samarium-doped strontium titanate nanostructures under UV light. A structural and electronic understanding*. Phys. Chem. Chem. Phys. **12**, 7566 (2010).
- [31] P. García-Fernández, M. Verissimo-Alves, D. I. Bilc, P. Ghosez, and J. Junquera. *First-principles modeling of the thermoelectric properties of $\text{SrTiO}_3/\text{SrRuO}_3$ superlattices*. Physical Review B: Condensed Matter and Materials Physics **86**, 085305 (2012).
- [32] R. Viana, P. Lunkenheimer, J. Hemberger, R. Böhmer, and A. Loidl. *Dielectric spectroscopy in SrTiO_3* . Physical Review B: Condensed Matter and Materials Physics **50**, 601 (1994).
- [33] S. M. Sze and K. N. Kwok. *Physics of Semiconductor Devices*. Wiley-Interscience.
- [34] M. Brahmia, B. Bennecer, and A. Hamidani. *Electronic and optical properties of the orthorhombic compounds FeX_2 ($X = \text{P}, \text{As}$ and Sb)*. Materials Science and Engineering: B **178**, 1249 (2013).